

Network-based disease fingerprinting with neuroinflammation PET imaging

Received: 4 December 2025

Accepted: 23 March 2026

Published online: 10 April 2026

Cite this article as: Barzon L., Maccioni L., Carranza Mellana M. *et al.* Network-based disease fingerprinting with neuroinflammation PET imaging. *J Neuroinflammation* (2026). <https://doi.org/10.1186/s12974-026-03788-1>

Leonardo Barzon, Lucia Maccioni, Michelle Carranza Mellana, Julia J. Schubert, Ludovica Brusaferrri, Oliver Cousins, Ivana Rosenzweig, Yuya Mizuno, Tiago Reis Marques, Neil A. Harrison, Tim Fryer, Edward T. Bullmore, Valeria Mondelli, Carmine Pariante, David Sharp, Gregory Scott, Joana B. Pereira, Oliver Howes, Vesna Sossi, Benedetta Bodini, Bruno Stankoff, Marco L. Loggia, Federico E. Turkheimer & Mattia Veronese

We are providing an unedited version of this manuscript to give early access to its findings. Before final publication, the manuscript will undergo further editing. Please note there may be errors present which affect the content, and all legal disclaimers apply.

If this paper is publishing under a Transparent Peer Review model then Peer Review reports will publish with the final article.

Network-based disease fingerprinting with neuroinflammation PET imaging

Leonardo Barzon¹, Lucia Maccioni¹, Michelle Carranza Mellana², Julia J. Schubert³, Ludovica Brusaferrri^{4,5}, Oliver Cousins³, Ivana Rosenzweig³, Yuya Mizuno^{3,6,7}, Tiago Reis Marques⁸, Neil A. Harrison⁹, Tim Fryer¹⁰, Edward T. Bullmore¹¹, Valeria Mondelli³, Carmine Pariante³, David Sharp¹², Gregory Scott¹², Joana B. Pereira¹³, Oliver Howes^{3,14}, Vesna Sossi¹⁵, Benedetta Bodini², Bruno Stankoff², Marco L. Loggia⁴, Federico E. Turkheimer³, Mattia Veronese^{1,3}

Affiliations:

¹Department of Information Engineering, University of Padova, Padova, Italy

²Paris Brain Institute, ICM, CNRS, Inserm, Sorbonne Université, Paris, France

³Institute of Psychiatry, Psychology and Neuroscience (IoPPN), King's College London, London, UK

⁴Departments of Radiology and Anesthesia, Critical Care and Pain Medicine, Massachusetts General Hospital, Harvard Medical School, Boston, MA, USA

⁵Computer Science and Informatics, School of Engineering, London South Bank University, London, UK

⁶South London and Maudsley NHS Foundation Trust, London, UK

⁷Department of Neuropsychiatry, Keio University School of Medicine, Tokyo, Japan

⁸Psychiatric Imaging Group, MRC London Institute of Medical Sciences (LMS), Hammersmith Hospital, Imperial College London, London, UK

⁹Cardiff University Brain Research Imaging Centre (CUBRIC), Cardiff University, Cardiff, UK

¹⁰Department of Clinical Neurosciences, School of Clinical Medicine, University of Cambridge, Cambridge, UK

¹¹Department of Psychiatry, School of Clinical Medicine, University of Cambridge, Cambridge, UK

¹²Division of Brain Sciences, Department of Medicine, Imperial College London, UK

¹³Division of Neuro, Department of Clinical Neuroscience, Karolinska Institute, Stockholm, Sweden

¹⁴Institute of Clinical Sciences (ICS), Faculty of Medicine, Imperial College London, London, UK

¹⁵Department of Physics and Astronomy, University of British Columbia, Vancouver, BC, Canada

Corresponding authors:

Leonardo Barzon

Department of Information Engineering, University of Padova

Via Gradenigo 6/B, 35122, Padova, Italy

+39 049 827 7640

leonardo.barzon.1@phd.unipd.it

<https://orcid.org/0009-0003-4517-221X>

Mattia Veronese

Department of Information Engineering, University of Padova

Via Gradenigo 6/B, 35122, Padova, Italy

+39 049 827 7654

mattia.veronese@unipd.it

<https://orcid.org/0000-0003-3562-0683>

Keywords: Neuroinflammation, PET, TSPO, Inter-regional similarity, Machine Learning

Abstract

Neuroinflammation is a hallmark of numerous neurodegenerative, psychiatric, and chronic pain disorders and can be assessed in vivo with 18 kDa translocator protein (TSPO) positron emission tomography (PET). However, conventional quantification methods of TSPO PET are limited and often overlook the spatial relationships between regional signals. The application of network-based approaches to TSPO PET imaging may provide a novel framework to capture disease-specific neuroinflammatory patterns. To address this question, here we developed a data-driven, network-based approach to generate individual brain-wide TSPO PET matrices, employing Euclidean distance to quantify inter-regional pharmacokinetics similarity. We applied this approach to a large multicenter dataset of 528 PET scans utilizing three different TSPO tracers ($[^{11}\text{C}]$ -PBR28, $[^{18}\text{F}]$ -DPA714, $[^{11}\text{C}]$ -PK11195), including healthy controls and patients with different diseases such as multiple sclerosis, traumatic brain injury, schizophrenia, depression, and chronic low back pain. Statistical modelling and machine learning classifiers were applied to evaluate the impact of experimental and biological factors on TSPO similarity patterns and to investigate their potential for capturing disease-specific signatures. TSPO similarity patterns demonstrated high biological specificity and reproducibility, with strong test-retest correlations (mean Spearman's $\rho = 0.84$). Average precision of disease classification exceeded chance performance by 23–89% across conditions and was driven by condition-specific regional hubs whose topological distributions closely mirrored disease pathophysiology. This specificity was further supported by minimal overlap in feature importance values across conditions. Altogether, our findings show that network-based analysis of human TSPO PET data can detect disease-specific neuroinflammatory signatures. Such methodologies underscore the biological significance of TSPO PET and enhance its translational value, supporting precision medicine strategies for neuroinflammatory disorders.

Introduction

Neuroinflammation is the immune response of the central nervous system (CNS) to injury, infection, or other challenges to the homeostasis (DiSabato et al., 2016) by microglia, astrocytes, endothelial cells, and infiltrating peripheral immune cells (Kreutzberg, 1996). While neuroinflammation plays a critical neuroprotective role in maintaining CNS homeostasis, particularly in the acute context, sustained or dysregulated activation can lead to detrimental effects and is increasingly recognized as a core pathological mechanism in a growing number of brain disorders. These include traumatic brain injury, multiple sclerosis, Alzheimer's disease, Parkinson's disease (Gerhard et al., 2006; Heneka et al., 2015; Schuitemaker et al., 2013; Tournier et al., 2020; Yong, 2022), major depressive disorder, schizophrenia (Aricioglu et al., 2016; Brites & Fernandes, 2015; Doorduyn et al., 2009; Müller, 2018; Troubat et al., 2021) and chronic pain syndromes (Loggia, 2024; Loggia et al., 2015; Torrado-Carvajal et al., 2021).

The 18 kDa translocator protein (TSPO) has emerged as a putative biomarker for neuroinflammation due to its elevated expression in activated glial and immune cells, particularly microglia, during CNS immune responses (Kim & Yu, 2015; Malpetti et al., 2024; Wijesinghe et al., 2025). Consequently, TSPO-targeted molecular imaging using positron emission tomography (PET) has become a widely utilized approach for *in vivo* quantification of neuroinflammatory processes (De Picker & Haarman, 2021; Jain et al., 2020; Werry et al., 2019). However, several methodological challenges have limited the clinical and translational potential of TSPO PET imaging as a biomarker for neuroinflammation (Turkheimer et al., 2015). Quantification using arterial input functions is limited by the invasiveness of arterial blood sampling and the complexity of measuring radioactivity and correcting for metabolites and protein binding (Tonietto et al., 2016), challenges further compounded by the low free plasma fraction of TSPO ligands (Albrecht et al., 2016). The use of ratio metrics (Lammertsma & Hume, 1996; J. Schubert et al., 2021) has demonstrated promise. However, identifying a pseudoreference region often requires substantial validation effort, as TSPO expression, although relatively low, is widespread across most brain cell types (Turkheimer et al., 2007). Additionally, in some cases the use of ratio metrics may reduce sensitivity to effects that are widespread across the brain. Together, these challenges have motivated the development of alternative modelling strategies that reduce invasiveness while maintaining biological specificity (Maccioni et al., 2025). Beyond technical limitations, most

TSPO PET studies have traditionally focused on either localised or widespread increases in magnitude of brain TSPO radiotracer binding, thus overlooking possible alterations in the network of inter-regional relationships that could reflect disease-specific neuroinflammatory profiles. Only few studies have examined how inflammation propagates across different brain regions (Gerhard et al., 2000; Radlinska et al., 2009), and systematic analyses of inter-regional TSPO signal similarity are still lacking. Analytical frameworks that capture the spatial organization of TSPO signals could therefore provide deeper insights into neuroinflammatory processes, revealing patterns that might be masked when regions are considered independently and informing more precise disease characterization and targeted therapeutic approaches.

In line with this, network-based methodologies applied to PET imaging appear particularly well-suited (Sala et al., 2023; Veronese et al., 2019). Traditionally based on group-level covariance analyses, the field has increasingly shifted toward new techniques capable of generating individual-level matrices that capture the tracer pharmacokinetics relationship between brain regions. These subject-specific network representations hold promise as biomarkers for disease diagnosis, stratification, and progression monitoring (Liu et al., 2016; Lu et al., 2024; Severino et al., 2025). Recently, Volpi and colleagues introduced a novel approach to assess the coherence of [^{18}F]-fluorodeoxyglucose (FDG) PET brain regional time-activity curves (TACs), employing Euclidean distance as an alternative to conventional correlation-based measures (Volpi et al., 2023). This method provides a valuable perspective on regional signal synchrony, potentially offering enhanced sensitivity to subtle network alterations often overlooked by traditional correlational metrics.

In this work, we propose a novel data-driven approach to generate single-subject TSPO similarity matrices that characterize the inter-regional relationships of TSPO PET pharmacokinetics within a network structure. Rather than relying on simple dynamic radioactivity measures, our method exploits a pre-defined set of biologically meaningful parameters that has been shown to summarize the inflammatory status of cerebral tissue (Maccioni et al., 2025), applying a metric derived from Euclidean distance to compute the similarity between regional inflammation.

We applied our framework to a large dataset comprising 528 TSPO PET scans acquired with three different radiotracers ([^{11}C]-PBR28, [^{18}F]-DPA714, [^{11}C]-PK11195), across multiple sites and scanners. This dataset included both healthy controls (HCs) and individuals with a broad spectrum of

acute and chronic neuroinflammatory conditions: psychiatric disorders associated with a mild inflammatory state (depression, DEP; schizophrenia, SCZ), conditions with acute central inflammation (multiple sclerosis, MS; traumatic brain injury, TBI), and patients with chronic low back pain (cLBP) as a model of inflammation with extra-cerebral origin. To our knowledge, no study has yet applied methodologies that take into account the similarity between different brain regions to human neuroinflammatory data at the single-subject level. Therefore, after evaluating the biological specificity and reproducibility of TSPO similarity matrices, we applied statistical and machine learning techniques to assess their sensitivity to both experimental and biological variables and evaluate their potential for disease fingerprinting or individual subject identification. The overarching hypothesis of this study is that this framework can uncover distinct network patterns reflective of unique inflammatory signatures, potentially distinguishing each condition in a data-driven and clinically meaningful way.

Methods

Study participants and image acquisition

The data analyzed in this work were gathered from *King's College London (KCL)*, *Imperial College London (ICL)*, *Athinoula A. Martinos Center for Biomedical Imaging, Massachusetts General Hospital (MGH)*, *Paris Brain Institute of Sorbonne University (ICM)*, and *University of British Columbia (UBC)* historical databases, including PET imaging data collected with three different TSPO radiotracers ($[^{11}\text{C}]\text{-PBR28}$, $[^{18}\text{F}]\text{-DPA714}$, and $[^{11}\text{C}]\text{-PK11195}$). Due to the influence of the TSPO gene rs6971 polymorphism on radiotracer binding affinity (Owen et al., 2012), all participants acquired with $[^{11}\text{C}]\text{-PBR28}$ or $[^{18}\text{F}]\text{-DPA714}$ were genotyped prior to imaging. Only high-affinity binders (HABs) and mixed-affinity binders (MABs) were included in the study. A comprehensive summary of the participants' characteristics is provided in **Table 1**. Technical specifications for the PET systems

utilized at each study site are detailed in the **Supplementary Material (Table S1)**. All procedures performed in studies involving human participants were in accordance with the ethical standards of the institutional and/or national research committee and with the 1964 Helsinki declaration and its later amendments or comparable ethical standards. Written informed consent was obtained from all individual participants included in the studies.

[¹¹C]-PBR28 datasets

KCL/ICL dataset

The dataset consists of the aggregation of 118 dynamic [¹¹C]-PBR28 PET scans from different imaging studies conducted at either at *KCL* and *ICL*, all acquired from the same facility and using the same imaging protocol. Specifically, dynamic scans were collected from 52 HCs, 15 individuals diagnosed with schizophrenia (SCZ), including 7 who underwent both a baseline and a blocking scan with XBD173 (Marques et al., 2021; Veronese et al., 2018), 14 participants with moderate-to-severe traumatic brain injury (TBI), and 5 patients with Alzheimer's disease (AD), who also completed retest scans. Full details regarding participant inclusion criteria and imaging procedures are available in the original publications (Bloomfield et al., 2016; Dahoun et al., 2019; Nair et al., 2016; Scott et al., 2018). In brief, all imaging sessions started with a low-dose computed tomography (CT) scan for attenuation and scatter correction, performed on a Siemens Biograph TruePoint PET/CT scanner (Siemens Medical Systems, Germany). This was followed by a 90-minute dynamic PET scan initiated immediately after a bolus injection of [¹¹C]-PBR28 (injected dose: 332.0 ± 26.9 MBq). The PET data were divided into 26 time frames (8×15s, 3×1 min, 5×2 min, 5×5 min, and 5×10 min), reconstructed using filtered back projection combined with 5 mm isotropic Gaussian smoothing, and corrected for random noise, attenuation, and scatter. Additionally, T1-weighted structural MR images were acquired using a Siemens 3-T scanner, either a Tim Trio or MAGNETOM Verio model.

MGH dataset

This dataset comprises a total of 94 [^{11}C]-PBR28 PET scans acquired at *MGH*, as part of multiple imaging studies (Albrecht et al., 2019; Alshelh et al., 2020; Morrissey et al., 2023; Torrado-Carvajal et al., 2021). The first subset of the data, including 27 HCs and 21 patients with chronic low back pain (cLBP), was collected using a hybrid PET-MR system consisting of an avalanche photodiode-based PET scanner integrated with a Siemens 3T Tim Trio MRI scanner (Bay 6). Following a 90-minute dynamic PET acquisition initiated immediately after the bolus injection of [^{11}C]-PBR28 (injected dose: 450.5 ± 63.0 MBq), data were reconstructed using the manufacturer's implementation of the 3D Ordinary Poisson Ordered-Subset Expectation Maximization (OP-OSEM) algorithm. The reconstructed dataset was then segmented into 28 temporal frames with the following durations: 8×10 s, 3×20 s, 2×30 s, 1×1 min, 1×2 min, 1×3 min, 8×5 min, and 4×10 min. Prior to radiotracer injection, a multi-echo MPRAGE structural MRI was acquired to enable anatomical localization and to generate attenuation correction maps for PET image reconstruction.

A second subset of data, including 26 HCs and 20 cLBP patients, was collected at *MGH* on a Siemens Biograph mMR whole-body PET-MR (Bay 7). Dynamic PET data were acquired over a 90-minute period following bolus injection of [^{11}C]-PBR28 (injected dose: 525.5 ± 52.9 MBq). The acquired data were divided into 28 temporal frames (duration: 8×10 s, 3×20 s, 2×30 s, 1×1 min, 1×2 min, 1×3 min, 8×5 min, and 4×10 min). Image reconstruction was performed using the Ordered Subset Expectation Maximization (OSEM) algorithm, employing 4 iterations, 21 subsets, and a Gaussian smoothing filter with a 3 mm FWHM. T1-weighted MR images were acquired for anatomical reference and for the generation of attenuation correction maps. Comprehensive information regarding participant eligibility and imaging procedures can be found in the original publications.

UBC dataset

This dataset comprises 21 [^{11}C]-PBR28 PET scans from 11 HCs and 10 individuals with SCZ, acquired with a GE SIGNA PET-MR scanner at *UBC*. Participants underwent a 90-minute PET acquisition following an intravenous bolus injection of [^{11}C]-PBR28 (injected dose: 565.4 ± 9.0 MBq). PET data were binned into 25 temporal frames with the following durations: 1×20 s, 2×10 s, 4×5 s, 3×1 min, 3×2 min, 8×5 min, and 4×10 min and subsequently reconstructed using PSF-HYPR4D-K-TOFOSEM

(Cheng et al., 2022). For anatomical localization and MRI-guided processing, all participants also underwent a high-resolution 3D T1-weighted MPRAGE sequence.

[¹⁸F]-DPA714 datasets

KCL dataset

The dataset includes 101 [¹⁸F]-DPA714 PET scans collected within the *Inflammatory Response In Schizophrenia (IRIS)*, carried out at the *Institute of Psychiatry, Psychology & Neuroscience, King's College London* (<https://clinicaltrials.gov/study/NCT03093064>). The dataset includes 39 HCs and 62 patients with first-episode psychosis (FEP) who remained symptomatic despite antipsychotic treatment. Each participant underwent a 60-minute dynamic PET acquisition following a bolus injection of [¹⁸F]-DPA714 (injected dose: 187.1 ± 6.5 MBq), performed on a 3 T SIEMENS Biograph mMR PET-MR scanner. The PET data were reconstructed into 26 frames with the following timing sequence: 1×60 s, 8×15 s, 3×1 min, 5×2 min, and 9×5 min. Additionally, all subjects received a baseline T1-weighted structural MRI scan (MPRAGE sequence) acquired on the same scanner.

ICM dataset

This dataset comprises a total of 118 [¹⁸F]-DPA714 PET scans acquired at ICM as part of multiple imaging studies. The first subset includes scans from 14 HCs, 7 of whom underwent a retest scan within a period of 82 to 321 days following the initial acquisition, and 38 patients with multiple sclerosis (MS), all acquired using a GE SIGNA PET-MR scanner at SHFJ-CEA in Orsay and at Pitie Salpetriere Hospital. PET data were acquired over a 90-minute period following intravenous bolus injection of [¹⁸F]-DPA714 (injected dose: 222.7 ± 23.4 MBq). Image reconstruction was performed using a 3D Ordinary Poisson Ordered Subset Expectation Maximization (OP-OSEM) algorithm with integrated point spread function (PSF) modelling. The reconstructed data were divided into 33 temporal frames with the following durations: 9×20 s, 3×1 min, 7×2 min, and 14×5 min. In addition, all participants underwent a high-resolution 3D T1-weighted MPRAGE MRI sequence for anatomical reference.

A second subset consists of 15 HCs, including 8 who completed a retest scan within a period of 5 to 67 days following the initial acquisition, and 36 MS patients. For each participant, [^{18}F]-DPA714 was administered intravenously as a slow bolus injection over a 1-minute period (injected dose: 196.3 ± 15.2 MBq). Dynamic PET data were acquired for 90 minutes on a High-Resolution Research Tomograph (HRRT, Siemens, Knoxville, TN, USA) at SHFJ-CEA in Orsay. PET images underwent corrections for attenuation, random events, and scatter, and were reconstructed using a 3D ordered-subset expectation maximization algorithm based on an Ordinary Poisson (OP-OSEM) statistical model. The resulting data were divided into 27 temporal frames (6×1 min, 7×2 min, and 14×5 min). A 3D Gaussian smoothing kernel with a 2 mm full width at half maximum (FWHM) was applied to account for the system's point-spread function. Additionally, each subject underwent a T1-weighted MPRAGE MRI scan, acquired either on a Philips Achieva 1.5 T system (Best, The Netherlands) or a Siemens Trio 3 T system (Erlangen, Germany).

[^{11}C]-PK11195 dataset

KCL dataset

The dataset comprises 76 dynamic PET scans with [^{11}C]-PK11195, collected as part of the Biomarkers in Depression study (BIODEP). It includes scans from 51 individuals with mild to moderate depression (DEP) and 25 matched HC participants. Further information on subject recruitment and clinical assessments can be found in previous studies (Turkheimer et al., 2021; Schubert et al., 2021). All participants underwent a 60-minute dynamic PET scan using a GE SIGNA PET/MR scanner (GE Healthcare, Waukesha, USA) following an intravenous bolus injection of [^{11}C]-PK11195 (injected dose: 366 ± 51 MBq). The data were divided into 17 frames (4×15 s, 4×1 min, 7×5 min, 2×10 min). Attenuation correction was performed using a multi-subject atlas approach optimized for the MRI brain coil (Burgos et al., 2014). Standard corrections for scatter, random events, and dead time were applied using the GE scanner software. Additionally, each subject underwent a high-resolution T1-weighted structural brain MRI (Brain Volume Imaging, BRAVO) during the PET acquisition.

Radiotracer	Site	Scanner	Group	Age (y)	Sex (M/F)	Affinity (HAB/MAB)
[¹¹C]-PBR28	KCL/ICL	Siemens Biograph TruePoint PET- CT	HC (n=72)	32 ± 13	50/22	50/22
			SCZ (n=15) +7 blocking	46 ± 10	12/3	13/2
			AD (n=5) +5 retest	82 ± 4	4/1	5/0
			TBI (n=14)	42 ± 14	12/2	9/5
	MGH (Bay 6)	PET-MR: PET within Siemens 3T Tim Trio MR	HC (n=27)	47 ± 13	13/14	17/10
			cLBP (n=21)	43 ± 14	10/11	17/4
	MGH (Bay 7)	Siemens Biograph mMR whole-body PET- MR	HC (n=26)	55 ± 15	12/14	13/13
			cLBP (n=20)	47 ± 17	9/11	11/9
	UBC	GE SIGNA PET- MR	HC (n=11)	35 ± 10	3/8	8/3
			SCZ (n=10)	35 ± 8	2/8	5/5
[¹⁸F]-DPA714	KCL	Siemens Biograph mMR PET-MR	HC (n=39)	29 ± 8	21/18	29/10
			FEP (n=62)	28 ± 8	41/21	41/21
	ICM (PET- MR)	GE SIGNA PET- MR	HC (n=14) + 7 retest	43 ± 13	9/5	8/6
			MS (n=38)	46 ± 10	16/22	18/20

	ICM (HRRT)	Siemens HRRT	HC (n=15) +8 retest	43 ± 13	6/9	7/8
			MS (n=36)	48 ± 11	15/21	21/15
^[11C] -PK11195	KCL	GE SIGNA PET- MR	HC (n=25)	37 ± 8	11/14	/
			DEP (n=51)	36 ± 7	15/36	/

Table 1. Demographic and clinical characteristics of participants

Acronyms: KCL, King’s College London; ICL, Imperial College London; MGH, Massachusetts General Hospital; UBC, University of British Columbia; ICM, Paris Brain Institute; HC, healthy control; SCZ, schizophrenia; AD, Alzheimer’s disease; TBI, traumatic brain injury; cLBP, chronic low back pain; FEP, first-episode psychosis; MS, multiple sclerosis; DEP, mild-to-moderate depression.

Data preprocessing and TACs extraction

Data were pre-processed at each neuroimaging centre using various combinations of in-house scripts and established analysis software, including the FMRIB Software Library (FSL, <http://www.fmrib.ox.ac.uk/fsl>), Statistical Parametric Mapping (SPM, <http://www.fil.ion.ucl.ac.uk/spm>), FreeSurfer (<https://surfer.nmr.mgh.harvard.edu>), and MIAKAT (Gunn et al., 2016). While specific software implementations varied across sites due to the retrospective nature of this data assembly, all pipelines were conceptually aligned to follow an identical processing sequence to ensure cross-site consistency. The pre-processing pipeline for all scans comprised motion correction of dynamic PET data (inter-frame re-alignment), generation of motion-corrected PET reference images, extraction of brain and grey matter masks from structural T1-weighted MRI, and registration of these masks to each subject’s native PET space. Additionally, the FreeSurfer APARC+ASEG neuroanatomical parcellation, which includes cortical regions from the Desikan-Killiany atlas and subcortical areas from the ASEG segmentation, was co-registered to the individual PET images. For subsequent analyses, a total of 87 ROIs were selected: 68 bilateral cortical regions, 16 subcortical regions, the bilateral cerebellar cortex, and the brainstem. Finally, ROIs mean regional time-activity curves (TACs) were computed for each subject. For MS patients, the preprocessing

pipeline incorporates a lesion inpainting step to enhance atlas coregistration and mitigate structural artifacts arising from lesions (see Chard et al., 2010 for further details).

Networks construction

The present method was inspired by recent molecular connectivity approaches based on Euclidean distance metrics applied to TACs (Volpi et al., 2023). However, rather than relying on full dynamic PET signals, our approach focuses on a reduced set of biologically meaningful regional parameters. For each scan, regional TACs were interpolated onto a common sparse time grid using linear interpolation with extrapolation. Then, for each region, a feature vector was constructed including standardized uptake values (SUV) at three representative time points (1.25, 13.5, and 50 minutes post-injection) and the regional K_1 parameter estimated with a single irreversible compartment model, employing an image-derived input function (IDIF) (Barzon et al., 2025; Maccioni et al., 2024). For full details on the IDIF extraction methodology and K_1 computation, see **Supplementary Material S.2**. These parameters were selected based on a recently proposed methodology for TSPO PET quantification (Maccioni et al., 2025), having been identified by a logistic regression model as the most informative for differentiating regions with high and low TSPO expression, thereby reflecting the inflammatory status of cerebral tissue. To account for inter-subject variability and ensure that each feature contributed equally to the calculation of the Euclidean distance, all features were standardized within each tracer group. This was achieved by applying a robust z-score transformation, calculated as the difference between each value and the group median, divided by the median absolute deviation. Individual TSPO PET similarity matrices were derived by computing, for each pair of regions, the normalized inverse Euclidean similarity between regional feature vectors, defined as

$$S_{ij} = \frac{1}{1 + d_{ij}}$$

where d_{ij} is the Euclidean distance between the feature vectors of ROI i and ROI j , computed as

$$d_{ij} = \sqrt{\sum_{k=1}^n (x_{ik} - x_{jk})^2}$$

with x_{ik} representing the standardized value of feature k within the feature vector of ROI i , and n being the total number of features in the vector. Higher values of S_{ij} indicate greater similarity between regional molecular profiles.

To assess the inter-subject consistency of network patterns, pairwise Spearman's correlations were computed between the upper triangular elements of each healthy subject's resulting similarity matrix.

Evaluation of biomarker biological specificity and reproducibility

The specificity of TSPO similarity matrices for the TSPO molecular target was assessed through a retrospective analysis of data acquired before and after pharmacological partial blockade of the target using the ligand XBD173 in a cohort of 7 SCZ patients (Veronese et al., 2018). Specifically, the median of the elements in the upper triangular portion of the connectivity matrices was compared before and after blocking using a one-tailed Wilcoxon signed-rank test, to test the hypothesis that target blockade would result in a flatter and more homogeneous signal distribution across the brain, thereby increasing the average similarity values between regions. One subject was excluded prior to the evaluation due to unexplainable variability in the baseline scan (Marques et al., 2021).

The reproducibility of TSPO similarity matrices was evaluated in cohorts for which test-retest scans were available, specifically 5 patients with AD acquired with [^{11}C]-PBR28 at *KCL* and 15 HCs scanned with [^{18}F]-DPA714 at *ICM*. Spearman's correlation was computed between the corresponding elements of the upper triangular portions of the test and retest similarity matrices. Additionally, edgewise intraclass correlation coefficients (ICCs; type ICC(3,1), two-way mixed-effects model, single measurement) were computed for each element of the similarity matrices across test and retest sessions. Finally, a fingerprinting analysis (J. Liu et al., 2018) was performed by testing the ability to correctly identify, for each test scan, its corresponding retest scan as the most similar in terms of correlation between TSPO similarity matrices.

Evaluation of technical and biological effects on TSPO similarity matrices

A set of statistical and machine learning methods was applied to healthy individuals to assess the potential influence of various factors on TSPO network features. Specifically, the effects of batch (a combination of scanner, site, and acquisition protocol), TSPO genotype, sex, age, and radiotracer dose-over-weight ratio (DW) were evaluated.

To independently assess the impact of site and scanner, we regressed out potential confounding variables, including sex, TSPO genotype, age, and radiotracer DW, by applying edge-wise linear models and retaining the residuals. These residuals were then visually inspected for clustering using Uniform Manifold Approximation and Projection (UMAP, McInnes et al., 2018). To quantitatively evaluate site-related effects, three machine learning classifiers—logistic regression with elastic net regularization, k-nearest neighbors, and support vector machines (with linear, polynomial, and radial basis function kernels)—were trained to predict site labels within each tracer group. The data were partitioned into training (70%) and testing (30%) sets. Within the training phase, features were standardized, and hyperparameters were optimized via 10-fold cross-validation (CV) and grid search. Model performance was evaluated on the held-out test set using balanced accuracy, with 95% confidence intervals estimated through 1000 bootstrap iterations.

The same framework was adopted to assess the effects of sex and TSPO genotype. Following batch effect regression, binary classification models were trained within each tracer cohort using the same set of classifiers and procedures.

Additionally, to simultaneously quantify the effects of all aforementioned technical and biological variables on TSPO networks, tracer-specific multiple linear regression models were applied to each edge value. For each regressor, the distribution of standardized beta coefficients across all edges was examined, and Cohen's d was computed to determine whether the overall effect of a given variable on similarity values was predominantly positive or negative, and thus whether the beta coefficients were, on average, significantly greater or less than zero.

Disease classification

Disease classification analyses were conducted using a one-vs-all approach, in which each diagnostic group was classified against all HC scans acquired with the same tracer. An exception was made for SCZ patients, who were pooled across tracers (including also individuals with FEP) and classified against a combined HC group from [^{18}F]-DPA714 and [^{11}C]-PBR28 cohorts. For each classification task, the dataset was randomly split into 70% for training and 30% for testing. The effects of batch, sex, TSPO genotype, age, and radiotracer dose-to-weight ratio were regressed out from the unique 3,741 unique network edge values using the previously described linear models. To prevent the removal of disease-related variance and avoid data leakage, confound correction models were fitted exclusively on the HCs in the training set and then applied to the entire dataset. Afterward, the resulting residuals were z-scored to allow direct comparison of model coefficients. Model training involved a stratified 10-fold CV on the training set, performed 10 times to enhance reliability. When class sizes were limited, stratified k -fold CV was employed, ensuring that each fold contained at least one individual from the positive class.

For this task, we selected a logistic regression model with L1 regularization for its interpretability and its ability to enable post-hoc identification of relevant features for classification through the examination of non-zero coefficients, while offering a fully data-driven approach that does not require prior feature selection. Model performance was evaluated using the Average Precision (AP) score, which corresponds to the area under the precision-recall curve. AP was chosen as it is threshold-independent and particularly well-suited for handling class imbalance, which was characteristic of the datasets. AP was used consistently as the scoring metric during CV for model selection and as the primary evaluation metric on the test set. Receiver operating characteristic area under the curve (ROC AUC) was also computed on the test set. The 95% confidence intervals for AP and ROC AUC were estimated using 1,000 bootstrap iterations.

To interpret model outputs and identify the most discriminative brain regions, regional importance scores were computed. Specifically, for each ROI, the importance score was quantified as the sum of the absolute values of the logistic regression coefficients associated with all network edges connected to that ROI. Moreover, to assess the distinctiveness of the network profiles associated with each

disease, pairwise Kendall's tau correlations were computed between the beta coefficients of the logistic regression models from each classification task. This analysis quantified the degree of overlap in feature importance patterns across diseases, providing a measure of how similar or distinct the discriminative network features were between different pathological conditions.

Finally, a multiclass logistic regression classifier with L1 regularization was trained using data from all tracers and centres to discriminate between the different disease groups. The same confound correction and training procedure described above was applied. Model performance was assessed on the test set using balanced accuracy, with 95% confidence intervals estimated as previously described.

Individual-level patient fingerprinting

Lastly, we investigated the feasibility of individual patient fingerprinting based on TSPO network profiles. To account for batch effects, a linear regression model was trained on healthy controls and subsequently applied to all subjects to remove the influence of batch, sex, TSPO genotype, age, and radiotracer dose-to-weight ratio. To assess inter-subject similarity, pairwise Spearman's correlations were then computed between the vectorized upper triangular elements of all subjects' similarity matrices. Each patient was assigned to the diagnostic group of the subject with whom they shared the highest correlation. A fingerprinting confusion matrix was generated to summarize classification performance, from which balanced accuracy and per-group recall were derived.

Given the potential risk that batch correction might inflate apparent disease-related effects—potentially due to the collinearity between disease status and batch membership— we repeated the fingerprinting analysis using the original, uncorrected network features within the [^{11}C]-PBR28 dataset from KCL, as this batch included more than one clinical group, namely SCZ and TBI. This sensitivity analysis ensured that fingerprinting performance was not artificially driven by overcorrection artifacts.

Software implementation

All network construction and statistical analyses were implemented in MATLAB R2022b (MathWorks). Machine learning models, including classification tasks and multiple linear regressions, were developed in Python (version 3.8.13) using the scikit-learn library (version 1.3.2) (Pedregosa et al., 2011). Analyses were performed on a Linux workstation equipped with an Intel Core i7 (10th Gen, vPro) processor with 16 logical cores and 32GB of RAM. Disease classification was the most computationally intensive step, with execution times ranging from a few minutes to approximately 10 minutes for the largest cohorts, depending on the training set size.

Results

TSPO network topology across subjects, scanners, and radiotracers in healthy individuals

Single-subject TSPO similarity matrices were computed by calculating the normalized inverse of the Euclidean distance between vectors of regional PET-derived features, including standardized uptake values at 1.25, 13.5, and 50 minutes post-injection, as well as the tracer blood-to-brain influx rate (K_1). Each network is uniquely represented by a matrix, where each element denotes the TSPO pharmacokinetic similarity between two regions of interest (ROIs). An illustrative example of the resulting matrix in a HC is presented in **Figure 1A**. These matrices exhibited consistent inter-subject patterns with comparable network profiles across HC individuals. Across-subjects average similarity matrices by site showed higher similarity among cortical regions than among subcortical regions or cortico-subcortical connections (**Figure 1B**). Remarkably, the matrices captured the expected correspondence between homologous cortical, subcortical, and cerebellar regions across hemispheres, as evidenced by prominent secondary diagonals.

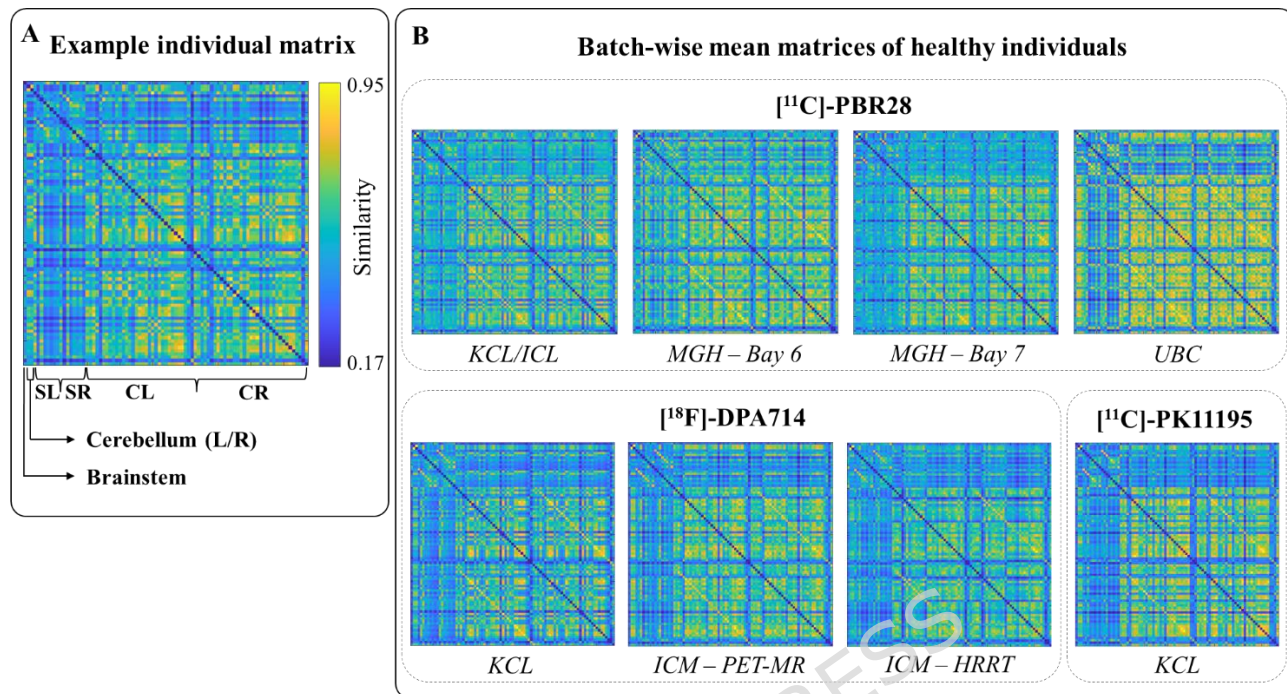


Figure 1. TSPO similarity matrices and cross-centre comparison. Panel A displays a representative similarity matrix from a HC subject, with axis labels showing the organization of ROIs. Panel B shows the average similarity matrices across healthy individuals for each dataset/batch. Acronyms: KCL, King’s College London; ICL, Imperial College London; MGH, Massachusetts General Hospital (Bay 6 and Bay 7 indicate the two scanners); UBC, University of British Columbia; ICM, Paris Brain Institute (PET-MR and HRRT indicate the two scanners); ROI, region of interest; L, left; R, right; CL, cortical left; CR, cortical right; SL, subcortical left; SR, subcortical right.

TSPO network patterns appeared generally consistent across different centres. This was reflected by the generally moderate correlations in the inter-subject correlation matrix (**Figure 2**), with a global median Spearman’s correlation ($\rho \pm$ median absolute deviation) of 0.47 ± 0.09 . The highest correlations were typically observed within centres and among scans acquired with the same radiotracers. Specifically, intra-tracer Spearman’s ρ was 0.50 ± 0.13 for $[^{11}\text{C}]\text{-PBR28}$, 0.53 ± 0.19 for $[^{18}\text{F}]\text{-DPA714}$, and 0.69 ± 0.07 for $[^{11}\text{C}]\text{-PK11195}$. Inter-tracer similarity was lower, with values of 0.42 ± 0.12 for $[^{18}\text{F}]\text{-DPA714}$ vs $[^{11}\text{C}]\text{-PBR28}$, 0.47 ± 0.10 for $[^{18}\text{F}]\text{-DPA714}$ vs $[^{11}\text{C}]\text{-PK11195}$, and 0.49 ± 0.10 for $[^{11}\text{C}]\text{-PBR28}$ vs $[^{11}\text{C}]\text{-PK11195}$. Nonetheless, the relatively high inter-subject similarity suggests there were comparable biological patterns across tracers and centres.

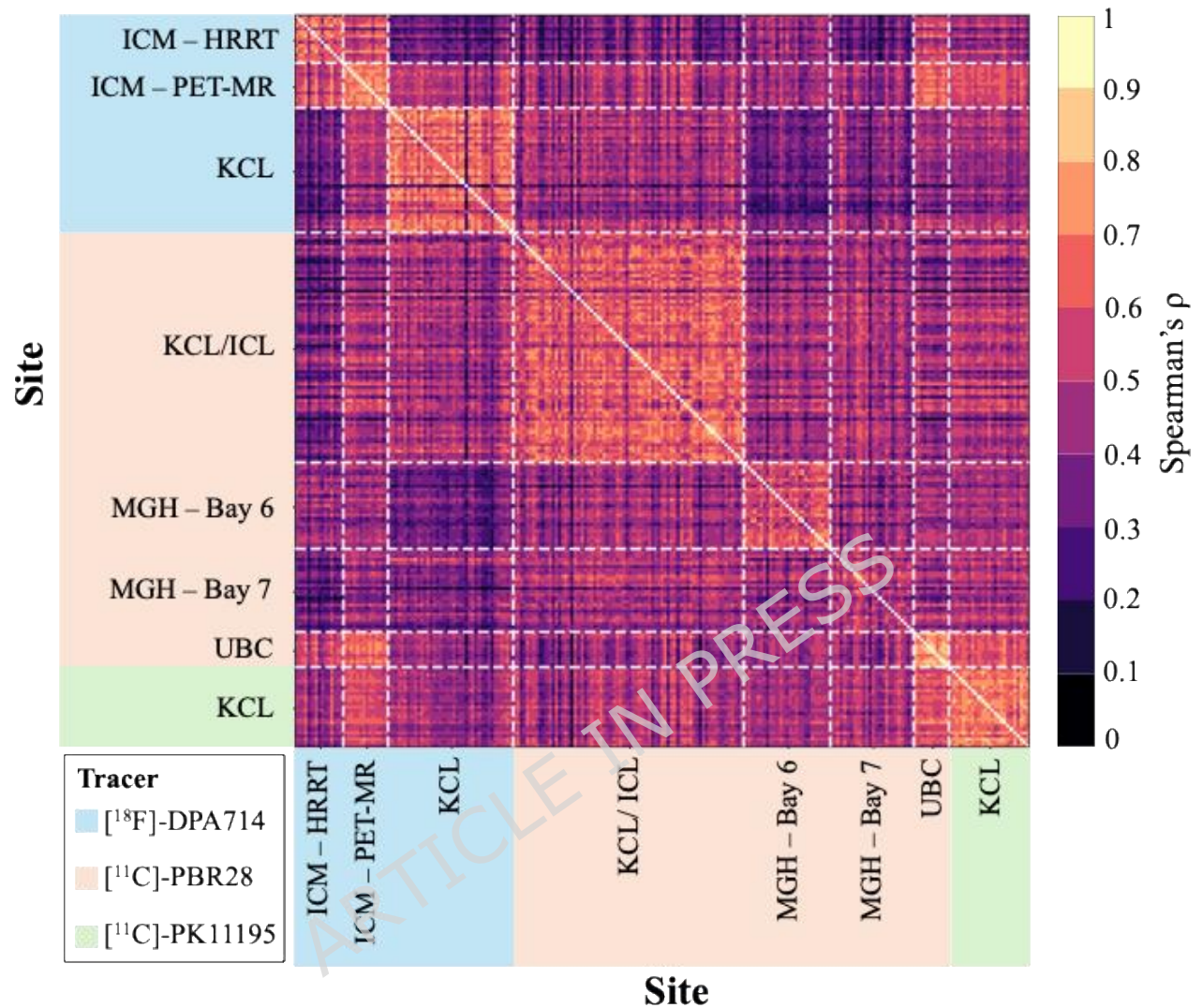


Figure 2. TSPO similarity matrices inter-subject correlations. The figure represents the inter-subject correlations of network patterns, calculated as Spearman's correlation coefficients between the unique off-diagonal elements of the TSPO similarity matrices across healthy controls; tracer and site groupings are also indicated. Acronyms: KCL, King's College London; ICL, Imperial College London; MGH, Massachusetts General Hospital (Bay 6 and Bay 7 indicate the two scanners); UBC, University of British Columbia; ICM, Paris Brain Institute (PET-MR and HRRT indicate the two scanners).

TSPO networks are biologically specific and reproducible

The biological specificity of the TSPO similarity matrices was assessed by comparing network patterns before and after partial pharmacological blockade of TSPO target with XBD173 injection in a cohort of 6 SCZ patients (Marques et al., 2021; Veronese et al., 2018). As expected, after pharmacological blocking, we observed higher average inter-regional similarity values due to a flatter and more homogeneous distribution of signal across brain regions (**Figure 3A**; see **Supplementary Figure S3** for baseline and post-blocking similarity distributions). A one-tailed Wilcoxon signed-rank test confirmed a significant increase in median similarity after blocking (mean percentage increase 8.3%; $P = 0.02$).

To assess network reproducibility, we used two test-retest datasets: 5 patients with Alzheimer's disease (AD) scanned twice with [^{11}C]-PBR28 (within ~12 weeks) and 15 HC subjects scanned twice with [^{18}F]-DPA714 (within 5 to 321 days). We observed strong Spearman's correlations between the unique off-diagonal elements of the test and retest similarity matrices in both datasets (mean \pm SD: 0.85 ± 0.03 in AD patients and 0.83 ± 0.08 in HCs). The edge-wise intraclass correlation coefficients (ICC), computed for each matrix element and summarized as median \pm median absolute deviation, indicated good reliability in AD patients (0.78 ± 0.14) and moderate reliability in HCs (0.53 ± 0.14). Representative test-retest similarity matrix pairs and the edge-wise ICC matrices for both cohorts are illustrated in **Supplementary Figure S4**. Finally, network fingerprinting potential (J. Liu et al., 2018) was evaluated in terms of its accuracy in identifying, for each test scan, the corresponding retest scan according to the correlation between test and retest TSPO similarity matrices. Accuracy reached 100% in the AD cohort and 93.3% in the HCs cohort, with only one test scan for which the retest scan was the second-most similar rather than the top match (**Figure 3B**).

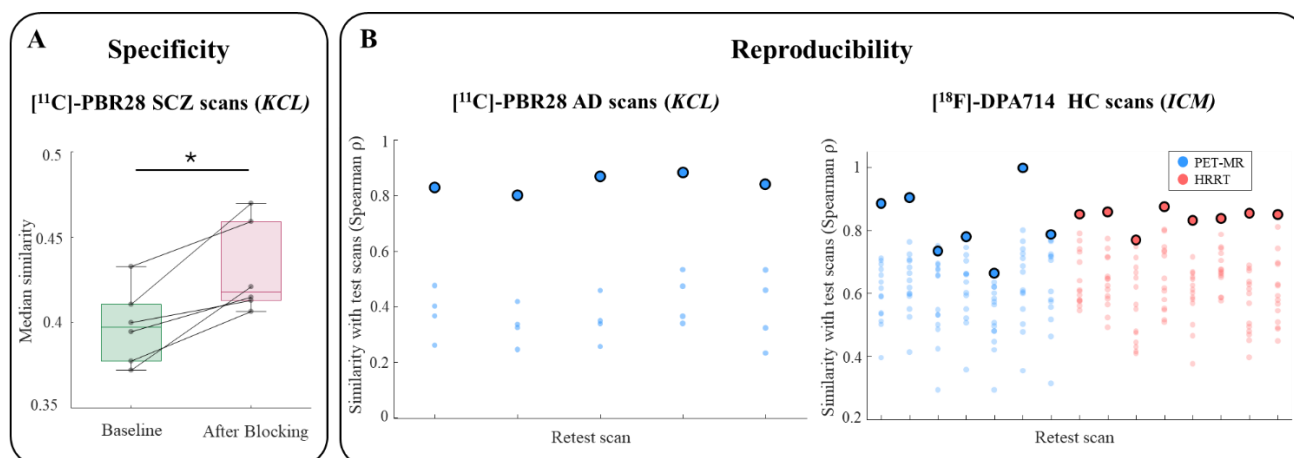


Figure 3. Biological specificity and reproducibility of the network-based methodology. Panel A displays the distribution of median inter-regional similarity values before and after TSPO binding blockade with XBD173 in individuals with SCZ scanned using [^{11}C]-PBR28 at *KCL*. Boxplots denote the median and interquartile range (IQR), with whiskers extending to the minimum and maximum values within $1.5 \times \text{IQR}$. A one-tailed Wilcoxon signed-rank test revealed a statistically significant reduction following blockade (* indicates $P < 0.05$). Panel B presents test-retest results from the AD patients scanned with [^{11}C]-PBR28 at *KCL*, and the HCs acquired with [^{18}F]-DPA714 at *ICM*. Each dot represents the Spearman's rho between the edge values of a given retest scan and those of all test scans within the corresponding site. The highlighted dot indicates the correlation between the test and retest scans of the same individual. Acronyms: SCZ, schizophrenia; AD, Alzheimer's disease; *KCL*, King's College London; *ICM*, Paris Brain Institute (PET-MR and HRRT indicate the two scanners).

Effects of technical and biological variability on TSPO similarity matrices

The sensitivity of TSPO similarity matrices to various experimental and biological variables was evaluated in healthy control subjects by investigating possible batch effects due to scanner and acquisition protocol differences, as well as possible effects of age, sex, genotype (specifically the TSPO gene rs6971 polymorphism, which affects the binding affinity of second-generation TSPO radiotracers (Owen et al., 2012)), and radiotracer DW. First, machine learning classifiers were applied to test whether we could predict acquisition site, sex, and TSPO binding affinity from individual TSPO similarity matrices. The different sites were indeed classified with highest accuracy for both [^{11}C]-PBR28 and [^{18}F]-DPA714 (balanced accuracy > 0.89), while sex and TSPO genotype were classified with moderate (balanced accuracy range: 0.51–0.68 for genotype, 0.63–0.75 for sex), showing variable performance for the three tracers (**Table 2**).

Tracer	Target variable	Best model	Balanced accuracy
$[^{11}\text{C}]$ -PBR28	Batch	KNN	0.89 [0.79, 0.98]
	Sex	KNN	0.63 [0.49, 0.77]
	Genotype	KNN	0.51 [0.35, 0.68]
$[^{18}\text{F}]$ -DPA714	Batch	KNN	0.94 [0.86, 1.00]
	Sex	LR	0.71 [0.52, 0.91]
	Genotype	SVM	0.68 [0.45, 0.90]
$[^{11}\text{C}]$ -PK11195	Sex	KNN	0.75 [0.38, 1.00]

Table 2. Classification performance for batch, sex, and TSPO genotype prediction. *Best model* refers to the classifier achieving the highest balanced accuracy on the test set. Classifiers include k-nearest neighbour (KNN), logistic regression (LR), and support vector machine (SVM) with linear kernel. Balanced accuracy on the test set is reported alongside corresponding 95% confidence intervals from 1,000 bootstrap iterations.

A linear model was also fitted for each element of the upper triangular matrix (network edge) to quantify the effect of age, sex, binding affinity, and DW across subjects. The associations presented in **Figure 4A-D** were derived from a statistical model that accounted for batch effects. To visualize the magnitude of the technical variance that necessitated this correction, **Figure 4E** displays the UMAP projections of the data prior to site-harmonization, confirming that the batch effect was indeed the strongest covariate. Model coefficient estimates demonstrated a consistent effect of predictors across tracers as represented by the coherent sign of the Cohen's d of the model coefficients distribution relative to zero (**Figure 4A-D**). Specifically, a global higher inter-regional similarity was observed in males compared to females, reflected by positive Cohen's d values (Cohen's d [95% confidence interval (CI)]: 0.83 [0.79, 0.87] for $[^{11}\text{C}]$ -PBR28, 0.23 [0.20, 0.27] for $[^{18}\text{F}]$ -DPA714, 0.48 [0.44, 0.51] for $[^{11}\text{C}]$ -PK11195). Similarly, MABs exhibited higher overall similarity compared to HABs (Cohen's d [CI]: 0.64 [0.60, 0.67] for $[^{11}\text{C}]$ -PBR28, 1.90 [1.84, 1.95] for $[^{18}\text{F}]$ -DPA714). Conversely, increasing age was associated with reduced global coherence between regions (Cohen's d [CI]: -0.63 [-0.67, -0.60] for $[^{11}\text{C}]$ -PBR28, -0.79 [-0.82, -0.75] for $[^{18}\text{F}]$ -DPA714, -0.04 [-0.07, -0.01] for $[^{11}\text{C}]$ -PK11195).

The tracer DW showed positive effects on similarity for [^{11}C]-PBR28 (Cohen's d [CI]: 1.65 [1.60, 1.70]) and [^{11}C]-PK1195 (Cohen's d [CI]: 1.02 [0.98, 1.06]) tracers, whereas a moderately negative effect was observed for [^{18}F]-DPA714 (Cohen's d [CI]: -0.31 [-0.34, -0.28]).

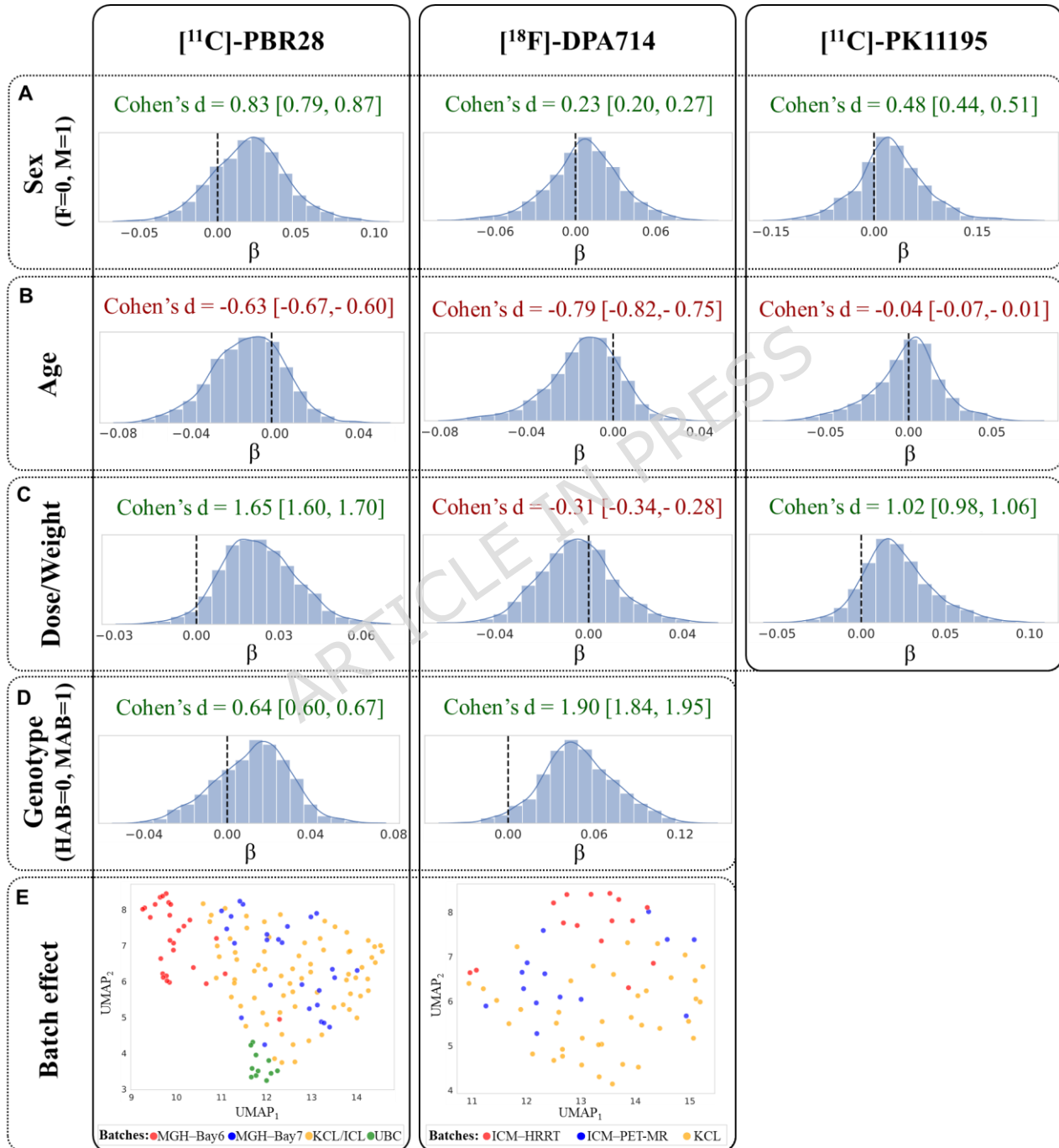


Figure 4. Global effects of demographic and experimental variables on graph edge values in healthy subjects. The first four rows (panels A-D) display the distributions of beta coefficients from linear regression models fitted at each

network edge, with sex, genotype, age, and DW as predictors. For each predictor, Cohen’s d relative to zero is reported together with 95% confidence intervals, while black dashed lines mark the zero-reference value. The bottom row (Panel E) illustrates batch effects, showing two-dimensional UMAP projections of network edge values after biological confound regression but before site-effect correction. Subjects are colour-coded according to batch membership (KCL: King’s College London; MGH, Massachusetts General Hospital (Bay 6 and Bay 7 indicate the two scanners); UBC, University of British Columbia; ICM, Paris Brain Institute (PET-MR and HRRT indicate the two scanners)).

Disease classification performance and feature importance

Binary logistic regression models with L1 regularization and stratified 10-fold cross-validation were trained to distinguish HCs from disease cohorts, using elements from the upper triangular portions of TSPO similarity matrices as predictors, after regressing out batch effects and potential confounders related to technical and biological variables. Classification performance, measured by Average Precision (AP) on the test set, consistently exceeded AP chance level—defined as the prevalence of disease-positive subjects in each dataset. Importantly, the lower bound of the 95% confidence interval remained above this threshold in all cases, demonstrating robust and reliable discrimination between patients and controls across conditions (**Table 3**).

Condition	Test set AP	AP chance level	Test set ROC AUC
TBI	1.00 [1.00, 1.00]	0.11	1.00 [1.00, 1.00]
DEP	0.96 [0.89, 1.00]	0.65	0.92 [0.78, 1.00]
MS	0.81 [0.66, 0.97]	0.52	0.85 [0.71, 0.96]
cLBP	0.51 [0.37, 0.79]	0.24	0.81 [0.68, 0.91]
SCZ	0.70 [0.57, 0.84]	0.47	0.74 [0.61, 0.87]

Table 3. Disease classification performance. For each condition test set AP, AP chance level, and test-set ROC AUC are reported, with 95% confidence intervals from 1,000 bootstrap iterations. Acronyms: AP, average precision; ROC AUC,

receiver operating characteristic area under the curve; TBI, traumatic brain injury; DEP, mild-to-moderate depression; MS, multiple sclerosis; cLBP, chronic low back pain; SCZ, schizophrenia

The contribution of each brain anatomical region to the classification was quantified by summing the absolute values of the logistic regression coefficients corresponding to the region edges. For every condition, the regions with the highest importance scores were distinct and disease-specific (**Figure 5A-E**). The top three contribution regions for each condition, alongside their importance score, were: left lateral orbitofrontal area (2.97), left rostral anterior cingulate area (2.69) and medial orbitofrontal area (2.28) for TBI; right and left putamen (2.13 and 1.88, respectively) and left thalamus (1.52) for MS; left accumbens area (2.55), right caudal anterior cingulate area (2.44) and left bankssts area (2.31) for cLBP; left putamen (1.79), right pallidum (1.53) and left frontal pole area for SCZ; right caudal middle frontal area (0.75), left rostral anterior cingulate area (0.67), and left pars opercularis area (0.50) for DEP. Consistent with disease specificity, Kendall's tau (τ) correlations between feature importance values (i.e., logistic regression beta coefficients) were generally low across conditions, with a maximum τ of 0.10 obtained for SCZ vs TBI (**Figure 5F**). The top network edges contributing to each disease classification are detailed in **Supplementary Material S.5**. Additionally, a multiclass logistic regression classifier, trained on data from all tracers and centres, successfully discriminated among the five disease groups (test set balanced accuracy [95% CI]: 0.81 [0.68, 0.90]). The corresponding confusion matrix, including per-group recall values, is provided in **Supplementary Material S.6**.

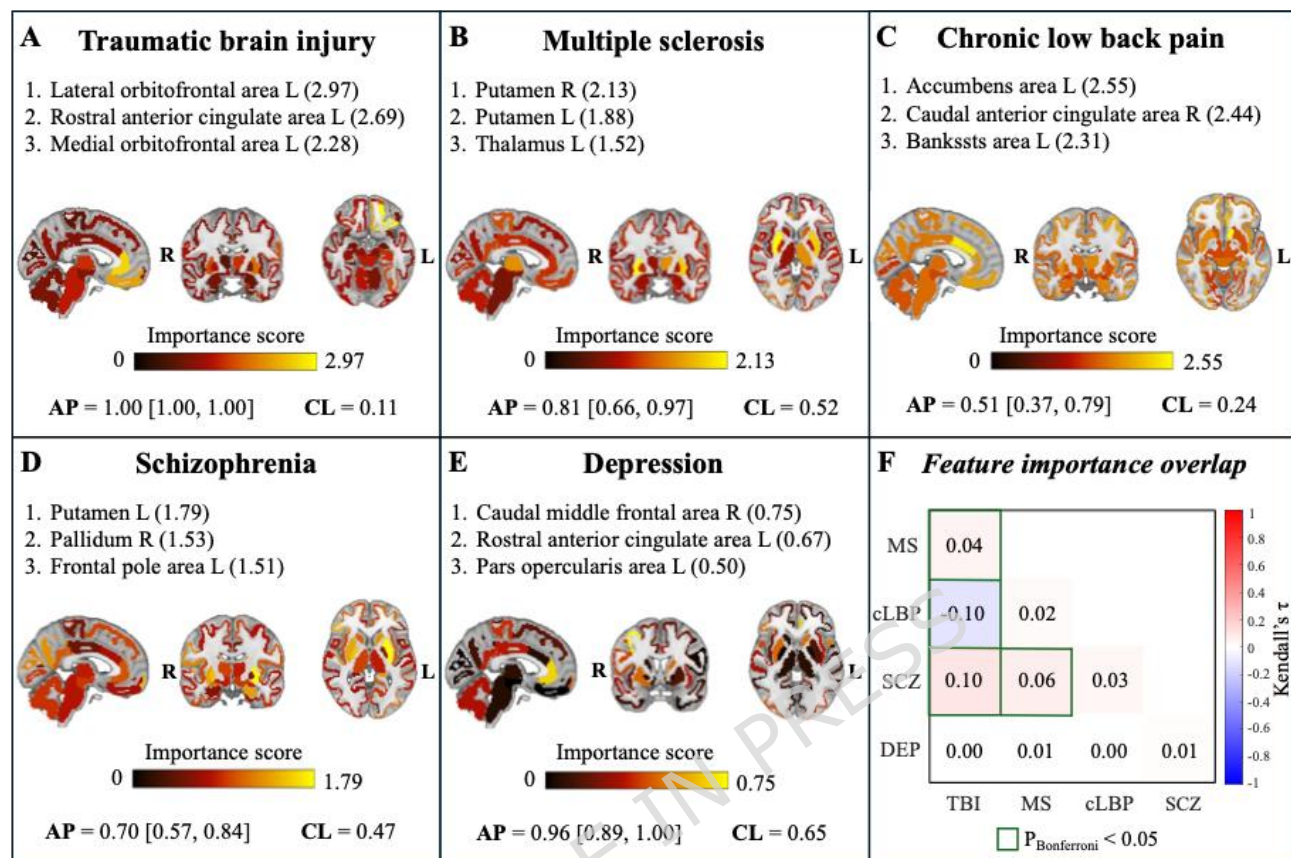


Figure 5. Regional contributions to diagnostic classification. In Panels A-E, brain maps show regional importance scores for disease classification, computed from the absolute values of logistic regression coefficients of network edges connected to each region. For each classifier, the three regions with the highest contributions and their corresponding score values are reported. Classification performance is summarized by the average precision (AP) score on the test set, reported together with the 95% confidence interval and the AP chance level (CL). Panel F shows the overlap between network edge logistic regression coefficients across conditions, quantified using Kendall correlation. Cells outlined in green indicate correlations that survived Bonferroni correction for multiple comparisons. Acronyms: MS, multiple sclerosis; cLBP, chronic low back pain; SCZ, schizophrenia; DEP, mild-to-moderate depression; TBI, traumatic brain injury; L, left; R, right.

Individual-level patient fingerprinting

Individual-level patient fingerprinting was performed by assigning each patient to the diagnostic group of the subject showing the highest pairwise Spearman correlation between their TSPO similarity matrices, after regressing out all confounding variables (site, sex, age, TSPO genotype, and DW) from the graph edges. Results of this analysis are presented in **Figure 6**. The inter-subject Spearman correlation matrix revealed distinct blocks of high correlations within diagnostic groups. The same pattern is represented in the fingerprinting confusion matrix, which demonstrates particularly high recall for MS (97.3%), TBI (92.9%), DEP (82.4%), and SCZ (83.9%), whereas a lower recall was observed for cLBP (53.7%). The overall fingerprinting balanced accuracy was 82.0%, exceeding the chance level of 20.0%. When the same analysis was replicated on the single [^{11}C]-PBR28 *KCL* dataset, without the necessity to regress out batch effects, the performances of SCZ and TBI patients classification remained above chance level (balanced accuracy: 73.1%; recall: 53.3% for SCZ, 92.9% for TBI).

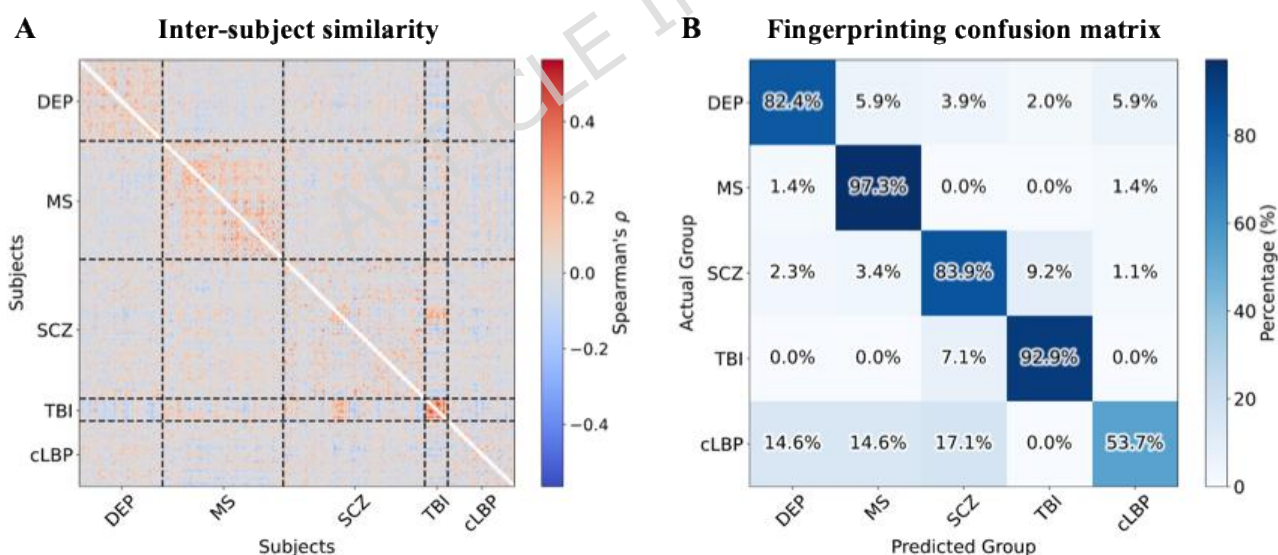


Figure 6. Results of individual patient fingerprinting analysis. Panel A presents the inter-subject similarity matrix for patients, computed using Spearman's ρ following the regression of all confounding variables (site, age, sex, TSPO genotype, and tracer dose-over weight ratio) from the graph edges. Panel B displays the fingerprinting confusion matrix, summarizing the identification accuracy of individual patients based on their network patterns. Acronyms: DEP, mild-to-moderate depression; MS, multiple sclerosis; SCZ, schizophrenia; TBI, traumatic brain injury; cLBP, chronic low back pain.

Discussion

In this study, we developed a novel analysis framework for TSPO PET, aimed at identifying disease-specific neuroinflammatory fingerprints. We derived TSPO similarity matrices by computing the distance between regional pharmacokinetic parameters, which have been shown to capture TSPO expression profiles (Maccioni et al., 2025). Our approach is conceptually similar to individual-level brain morphological similarity networks (Cai et al., 2023), which are typically constructed by calculating distances between regional magnetic resonance imaging (MRI)-derived features (Sebenius et al., 2023; H. Wang et al., 2016; Yu et al., 2018). Comparable methodologies have also been applied to PET-derived parameters across brain regions to generate individual-specific graphs (Protas et al., 2023; M. Wang et al., 2020; Zhu et al., 2022). However, to our knowledge, our study represents the first application of subject-level network analysis to TSPO PET imaging. Our method was applied to a large multicenter dataset comprising scans acquired across different facilities, using various tracers, PET scanners, and acquisition protocols. Despite this heterogeneity, the resulting individual TSPO PET pharmacokinetics similarity matrices demonstrated consistent patterns across healthy subjects. However, a clear batch effect was observed, highlighting the importance of accounting for site- and scanner-related variability when analyzing graphs derived from multicenter PET data.

The network-based analysis was performed on a set of cortical and subcortical regions, given the widespread expression of TSPO throughout the brain and its potential to be altered in pathological conditions (Nutma et al., 2021; Wijesinghe et al., 2025). A consistent pattern that emerged from the similarity matrices was a higher degree of similarity among cortical compared to subcortical regions or cortico-subcortical regions similarities. This may reflect a greater uniformity in the distribution and regulatory mechanisms of TSPO across cortical regions, as well as more consistent tracer pharmacokinetic characteristics within the cortex. Furthermore, this pattern could reflect the high functional connectivity characterizing the cortex, consistent with recent findings that TSPO PET spatial covariance partially mirrors functional connectivity (Rauchmann et al., 2022). Additionally, this effect might be partly driven by technical factors such as a higher signal-to-noise ratio of the ROI average TSPO PET signal in cortical areas compared to deep brain structures, which could enhance the

detectability of regional relationships. Importantly, the similarity matrices reliably captured the correspondence between homologous regions across the two hemispheres, further supporting a biological interpretation of the identified patterns and the sensitivity of the approach to meaningful inter-regional connections.

Notably, the observed inter-regional similarity pattern was consistent across tracers. This is particularly relevant because, despite the nominally identical target, these radioligands differ in affinity and pharmacokinetic properties (Rizzo et al., 2019). Nevertheless, a well-defined spatial organization was maintained, consistently replicated beyond the technical and experimental differences between studies. Such stability is likely related to the within-subject reproducibility, which, despite moderate ICC values in HCs and limited sample sizes, remains sufficient to enable accurate individual test-retest fingerprinting.

The biological specificity of the proposed approach was validated on pharmacological blocking data, showing a significantly increased inter-regional similarity after target blocking, reflecting a flatter and more homogeneous distribution of signal across brain regions. This effect, albeit observed in a small sample size, is likely due to the predominance of non-specific over specific signal following target occupancy, although the block was not complete (Marques et al., 2021; Veronese et al., 2018), possibly limiting the magnitude of the observed increase.

The ability of TSPO similarity matrices to identify disease-specific signatures was explored across a wide spectrum of neuroinflammatory conditions. These ranged from neuropsychiatric disorders such as DEP and SCZ, to diseases characterized by acute neuroinflammation, such as MS, and TBI, as well as a condition involving peripheral pathology (cLBP). By employing machine learning classifiers, we demonstrated the potential of TSPO PET network-based features to reliably distinguish patients affected by these conditions from healthy controls. Notably, the brain regions contributing most to disease classification closely reflect the known pathophysiological mechanisms of each disorder, highlighting the disease-specific nature of the identified patterns. To support the biological relevance of the data-driven findings, homologous bilateral regions frequently appear among the top contributors to disease classification, underscoring the robustness and value of these results. Remarkably, the emergence of disease-relevant patterns from the network-based analysis may suggest that TSPO PET imaging possesses disease specificity, further reinforcing its biological relevance. However, it is

important to acknowledge that these inter-regional similarity patterns could reflect a variety of underlying biological factors, and this study is not equipped to disentangle or attribute them to specific mechanisms. Such patterns may capture a range of processes, including the spreading of activated microglia, structural alterations, or structural and functional disconnections associated with neuroinflammatory states. Therefore, while these network-derived features have demonstrated robust biological relevance, their exact neurobiological basis remains to be fully elucidated. The following disease-specific discussion will further explore these potential interpretations in detail.

Regarding TBI, our study included patients who had experienced moderate-to-severe traumatic events. By nature, this population is heterogeneous, as the type and extent of injury vary according to the trauma mechanism. However, concussions, a significant part of TBI, are often associated with frontal lobe involvement due to the characteristic back-and-forth movement of the brain within the skull (Malloy & Aloia, 1998). Typically, the primary impact initiates a cascade of secondary biochemical processes, including inflammation, predominantly affecting the injury site and adjacent tissues, though neurodegeneration can also extend to distant brain regions (Borlongan et al., 2015). In this group, our analysis revealed prominent involvement of frontal regions, particularly the orbitofrontal cortex, along with subcortical structures such as the putamen. These hubs are highly consistent with the known pathophysiology of TBI, as frontal and subcortical areas are especially susceptible to damage following head trauma. Lesions in these regions have been associated with disruptions in frontal-subcortical circuits, encompassing the orbitofrontal, dorsolateral, and medial frontal cortices, together with the thalamus and striatum, including the putamen (McAllister, 2011).

In MS, our analyses identified the bilateral putamen and thalamus as the principal regional hubs. Notably, putaminal atrophy has been consistently reported in MS, beginning shortly after the onset of clinical symptoms and, in some cases, even preceding them by years, with a progressive and degressive trajectory over the disease course (Krämer et al., 2015). Similarly, thalamic degeneration is a well-established feature of MS and represents one of the earliest neuroanatomical changes (Azevedo et al., 2018). Both structures have been shown to predict disease conversion and future disability (Clarke et al., 2022). Importantly, the thalamus serves as a critical hub for cortico-subcortical communication, and alterations in thalamo-cortical functional connectivity have been associated with disease progression and clinical severity in MS (Y. Liu et al., 2015; Schoonheim et al., 2022). Recent evidence has further linked thalamic atrophy to disruptions in thalamo-cortical white matter pathways and,

notably, to alterations in microglial activity, including changes in cell density and morphology (Rodriguez-Mogeda et al., 2025). The thalamus has also been identified as a site of increased TSPO binding in MS patients compared to healthy individuals, as demonstrated by PET imaging studies (Laaksonen et al., 2023; Sucksdorff et al., 2020).

Regarding cLBP, the relatively modest performance observed for both disease classification and individual-level fingerprinting likely reflects the heterogeneous nature of the condition. Indeed, cLBP is an umbrella term that encompasses a broad range of underlying mechanisms. Our analyses revealed a substantially widespread involvement of both cortical and subcortical regions. However, the strongest contributors to disease classification were the accumbens area, the caudal and rostral anterior cingulate cortex (ACC), and the Banks of the superior temporal sulcus. The rostral ACC, as well as the lateral temporal cortex are part of the Default-Mode Network, a network that is highly implicated in the pathophysiology of chronic pain, including cLBP (Albrecht et al., 2021; Baliki et al., 2014; Loggia et al., 2013). The ACC represents a key hub within cortico-limbic circuits critically involved in the affective-motivational dimension and chronification of pain (Yang & Chang, 2019). Remarkably, the nucleus accumbens, which emerged as top contributor in the classification, is a key hub in pain processing and its alterations have been implicated in the transition to chronic pain (Chang et al., 2014; Harris & Peng, 2020; Makary et al., 2020). Evidence from TSPO PET imaging studies has demonstrated increased microglial activation in cLBP, particularly within the paracentral lobule, postcentral gyrus, and thalamus (Loggia et al., 2015). Although the main hubs identified by our network-based analysis did not directly overlap with these established neuroinflammatory regions, this discrepancy suggests that the computed network features may capture broader disease-related alterations beyond localized inflammation, potentially reflecting structural and functional reorganization associated with the pathological processes.

In the case of SCZ, our work revealed prominent involvement of the striatum — specifically the putamen and pallidum — alongside frontal cortical areas. The striatum has long been implicated in the pathophysiology of psychosis, primarily due to its central role in dopaminergic and glutamatergic dysregulation (O. D. Howes et al., 2024). Elevated presynaptic dopamine synthesis capacity and abnormal dopamine release in the striatum are replicated findings in schizophrenia research and are thought to underlie positive psychotic symptoms such as hallucinations and delusions (McCutcheon et al., 2019). Additionally, disruptions in glutamatergic transmission within striatal circuits have been

proposed to further exacerbate these dopaminergic abnormalities, creating a dysregulated cortico-striatal-thalamic loop (O. Howes et al., 2015; McCutcheon et al., 2020). Numerous studies also report structural and functional abnormalities in frontal cortical regions in schizophrenia, including some that have associated frontal abnormalities with cognitive deficits and negative symptoms (DeLisi et al., 2006; Mubarik & Tohid, 2016). Meta-analyses of PET studies have found evidence for altered TSPO in frontal cortex in schizophrenia relative to controls, albeit the direction of group differences may depend on the outcome measure used (Marques et al., 2019). Our findings extend these prior findings and other evidence for glial cell abnormalities in schizophrenia to show that the inter-regional similarity of TSPO measures also differentiates people with schizophrenia from controls. These findings are consistent with the hypothesis that glial cell abnormalities lead to aberrant synaptic pruning in schizophrenia (O. D. Howes & Onwordi, 2023).

Regarding depression, our findings highlight a predominant involvement of frontal regions, particularly the caudal middle frontal area, the ACC, and the pars opercularis. Notably, these regions have all been shown to exhibit structural alterations in affected individuals (Leung et al., 2009; Schmaal et al., 2017; Suh et al., 2019). Alterations in frontal lobe volume and morphology, along with dysfunction of frontal-subcortical circuits, have been associated with the disorder (Zhang et al., 2018). Frontal regions play a key role in mood regulation and have been consistently implicated in depression (Goldin et al., 2008; Talbot & Cooper, 2006). Remarkably, the prefrontal cortex and ACC have been identified as regions exhibiting elevated microglial activation in individuals with depressive disorder (Holmes et al., 2018; Richards et al., 2018; J. J. Schubert et al., 2021; Setiawan et al., 2018).

Finally, our study explored the potential of individual-level patient fingerprinting. The analysis revealed above-chance performance levels, suggesting that condition-specific network signatures may transcend the group level, remaining detectable at the single-subject level. It is important to acknowledge, however, that the batch correction model likely influenced patient fingerprinting performance, potentially leading to overestimation for groups such as DEP and cLBP, which were the only diagnostic categories within their respective batches. Nevertheless, the good segregation achieved for MS patients, despite originating from different scanners and acquisition protocols, provides further evidence supporting the value of this approach for patient-level fingerprinting. Moreover, uncorrected graph elements from the [^{11}C]-PBR28 KCL/ICL dataset demonstrated good individual fingerprinting capacity, with performance consistently above chance. Particularly noteworthy are the stable

performances observed for TBI patients, who, despite being intrinsically heterogeneous, exhibited remarkably similar molecular network patterns. Importantly, these findings underscore the intrinsic value that network-derived representations could provide in neuroimaging for individual-level fingerprinting and precision medicine. The specificity of PET signal, combined with the inherently multivariate nature of network-based approaches, enables the detection of subject-specific patterns that may extend beyond the capabilities of traditional univariate neuroimaging analyses. This potential attests the robustness and translational relevance of this and comparable frameworks for delineating individualized signatures, in line with previous evidence across distinct disease contexts (Severino, Peretti, et al., 2025)

We acknowledge that the proposed methodology has some limitations. First, our selection of meaningful TSPO PET parameters to construct regional feature vectors was guided by previous research (Maccioni et al., 2025) and is therefore subject to the limitations of that original study. In particular, the parameter selection was optimized only for [^{11}C]-PBR28 and applied without tailored calibration for [^{11}C]-PK11195 and [^{18}F]-DPA714. While adopting standardized timepoints facilitates methodological consistency, this reliance on parameters originally tailored to [^{11}C]-PBR28 kinetics represents a limitation, as it might not perfectly account for the subtle kinetic variations inherent to other radioligands, potentially impacting the generalizability of the feature extraction process. Additionally, our estimation of the K_I parameter, using a blood-free approach, was affected by the inherent limitations of the IDIF methodology (Maccioni et al., 2024; Volpi et al., 2023). Moreover, the retrospective nature of the study led to the inclusion of highly heterogeneous data. TSPO similarity matrices from healthy controls across different sites and scanners exhibited consistent spatial patterns, demonstrating the robustness of the methodology in handling heterogeneity. Nevertheless, the matrices remained sensitive to batch effects, likely reflecting differences in scanner models, image reconstruction methods, and acquisition protocols. Variations in acquisition protocols and tracer administration across PET centres can subtly alter tracer kinetics. Consequently, even after interpolating and standardizing TACs, signals may correspond to slightly different physiological states, affecting inter-regional distances. Differences in image reconstruction and scanner resolution likely further influence similarity calculation, but modelling these effects was not possible due to the lack of access to raw data. Furthermore, SUV was used rather than Standardized Uptake Value Ratio (SUVR) to construct regional feature vectors, as identifying a consistent reference region is unfeasible in a trans-

diagnostic study where regional involvement varies significantly across different pathologies. While this approach was essential to avoid introducing systematic biases through unreliable pseudo-reference regions, future investigations in more homogeneous cohorts could explore this or other within-subject feature normalization strategies to focus exclusively on inter-regional dependencies by eliminating global scaling effects. In addition, biological and experimental factors also influenced inter-regional similarities. Males exhibited higher similarity than females, consistent with sex-dependent differences in tracer delivery and binding (Barzon et al., 2025; Laaksonen et al., 2024; Tuisku et al., 2019). MABs showed higher global similarity than HABs, reflecting their greater proportion of non-specific binding and resulting in flatter spatial signal distributions. Conversely, similarity decreased with age, in line with increased heterogeneity of TSPO signal and loss of inter-regional coherence during aging (Farras-Permanyer et al., 2019; Fjell et al., 2017). Finally, increasing normalized dose was associated with higher inter-regional similarity for [¹¹C]-PBR28 and [¹¹C]-PK11195, likely reflecting progressive binding site saturation and signal homogenization, whereas for [¹¹F]-DPA714, higher doses were associated with a slight reduction in similarity. To account for these sources of variability, harmonization of inter-regional similarities was performed using regression models that assumed the effects of technical and biological variables to be linear. However, non-linear effects may also be present. More complex harmonization approaches were deemed unfeasible due to the limited overall sample size, particularly the small number of scans from certain sites. Nevertheless, an advantage of the linear regression model lies in the ease of estimating coefficients using only healthy individuals, allowing for the correction of confounding factors while preserving disease-related variability. Future investigations applying network-based methodologies within a controlled setting, where healthy and multiple disease populations are acquired under standardized conditions at the same site, are warranted to further validate their potential for both group- and individual-level fingerprinting. As a sensitivity analysis, we examined site-specific classifiers trained on patients and their matched healthy controls without applying the harmonization procedure. All models performed above chance level, with β coefficients showing significant correlations with those of the full harmonized model across all diseases (Kendall's tau, all $P < 0.001$; see **Supplementary Material Table S7** for full details). These results suggest that the main findings are robust to the confound correction strategy, although the full harmonized models remain more reliable, due to the larger training sample size, which yields more stable and robust estimates of the model coefficients. To further empirically validate the mitigation of technical bias, we conducted a classification analysis attempting to predict the site of origin (7-class

classification) from the data of healthy controls belonging to the [^{11}C]-PBR28 and [^{18}F]-DPA714 cohorts, following the regression of site-related and biological confounding effects. The same L1-regularized logistic regression architecture employed for the main disease classification tasks performed strictly at chance level (balanced accuracy = 0.14; 95% CI: [0.14, 0.17]), confirming that technical site-specific signatures were successfully decoupled from the biological signal. Furthermore, because a linear classifier, such as the logistic model utilized here, is mathematically incapable of exploiting non-linear dependencies, any residual non-linear scanner artifacts would not have been leveraged to drive diagnostic performance. Nevertheless, while the alignment of regional hubs with known pathophysiology offers promising indication, these sensitivity analyses do not entirely exclude the possibility that some topographical patterns may still reflect tracer- or scanner-specific characteristics rather than pure disease biology. Consequently, we maintain a conservative interpretation of these disease-specific fingerprints, pending further validation in standardized, prospective cohorts.

A further limitation arises intrinsically from TSPO PET imaging, particularly concerning the biological interpretation of regional TSPO density as a marker of neuroinflammation. Although widely used across clinical domains, TSPO lacks cellular specificity, being expressed in microglia but also astrocytes, some neurons, endothelial cells, and infiltrating immune cells (Vicente-Rodríguez et al., 2021; Wijesinghe et al., 2025). However, recent studies have suggested that, although TSPO overexpression does not always reflect proinflammatory microglial activation, regional TSPO elevations reliably correspond to increased densities of glial and immune cells (Nutma et al., 2023). Supporting this, post-mortem evidence shows positive correlations between ante-mortem TSPO PET binding and microglial TSPO levels, as well as CD68+ phagocytic microglia (Wijesinghe et al., 2025). Overall, previous findings indicate that TSPO PET offers a meaningful measure of neuroinflammatory load. Despite concerns regarding cellular specificity, our method leverages TSPO PET signals to generate robust neuroinflammatory fingerprints and to potentially reveal the spatial specificity of TSPO PET to different inflammatory conditions, in line with the expected alterations associated with these diseases. These demonstrated that beyond the magnitude of brain TSPO binding increases, alterations in the topological pattern of TSPO expression and in the network of inter-regional relationships of TSPO PET signal that could reflect disease-specific neuroinflammatory profiles. Importantly, the framework is potentially translatable to future molecular targets for

neuroinflammation and beyond, providing a versatile tool for both experimental and clinical investigations.

List of abbreviations

ACC: Anterior cingulate cortex

AD: Alzheimer's disease

AP: Average precision

cLBP: Chronic low back pain

CI: Confidence interval

CNS: Central nervous system

DEP: Mild-to-moderate depression

DW: Dose-to-weight ratio of radiotracer

HC: Healthy control

ICM: Paris Brain Institute

ICL: Imperial College London

KCL: King's College London

LR: Logistic regression

MGH: Massachusetts General Hospital

MS: Multiple sclerosis

PET: Positron emission tomography

ROI: Region of interest

SCZ: Schizophrenia

SVM: Support vector machine

TBI: Traumatic brain injury

TSPO: 18 kDa translocator protein

UBC: University of British Columbia

UMAP: Uniform Manifold Approximation and Projection

Conflict of Interest

Reis Marques, T. has received honoraria for speaking and chairing from Lundbeck, Janssen, Astellas and Viatrix and received honoraria to participate in advisory boards organized by Angelini Pharmaceuticals. He is an employee and shareholder of Pasithea Therapeutics.

Dr Mizuno has received consultant fees from Signant Health and WCG Clinical within the past three years.

Dr Howes has received research funding from and/or participated in advisory/ speaker meetings organised by Abbvie, Alkermes, Angellini, Autifony, Biogen, BMS (Karuna), Boehringer-Ingelheim, Delix, Eli Lilly, Elysium, Heptares, Global Medical Education, Invicro, Jansenn, Karuna, Lundbeck, Merck, Neumora, Neurocrine, Ono, Ontrack/ Pangea, Otsuka, Sunovion, Teva, Recordati, Roche, Rovi

and Viatrix/ Mylan. He was previously a part-time employee of Lundbeck A/v. Dr Howes and Dr. Veronese have a patent for the use of dopaminergic imaging.

Benedetta Bodini has received compensation for consulting services, speaking honoraria, participation in advisory boards or research support from Genzyme, Merck, Roche, Novartis, and Biogen (to the institution).

Bruno Stankoff has received research grants and personal fees for lectures from Roche, Novartis, and Merck-Serono, personal fees for lectures from Alexion, and Janssen.

All the other authors do not report any relevant conflict of interest.

Author Contributions

Conceptualization: LB, LM, MV

Methodology: LB, LM, MV

Investigation: LB

Visualization: LB, LM

Supervision: MV, BS, MLL, FET

Writing—original draft: LB, LM, MV

Writing—review & editing: LB, LM, MCM, JJS, LB, OC, IR, YM, TRM, NAH, TF, ETB, VM, CP, DS, GS, JBP, OH, VS, BB, BS, MLL, FET, MV

Funding

MV is supported by EU funding within the MUR PNRR “National Center for HPC, BIG DATA AND QUANTUM COMPUTING (Project no. CN00000013 CN1), by the Ministry of University and Research within the Complementary National Plan PNC DIGITAL LIFELONG PREVENTION - DARE (Project no PNC0000002_DARE), by Fondo per il Programma Nazionale di Ricerca e Progetti di Rilevante Interesse Nazionale (PRIN), (Project no 2022RXM3H7), and by the cascading grant “Q Amyloid – Quantitative Amyloid Imaging” under PNRR ECS00000017 “THE - Tuscany Health

Ecosystem,” Spoke 6: “Precision Medicine & Personalized Healthcare,” funded by the European Commission under the NextGeneration EU programme. LM is supported by Fondo per il Programma Nazionale di Ricerca e Progetti di Rilevante Interesse Nazionale (PRIN) (Project no 2022RXM3H7). JJS and FET are funded by the National Institute for Health and Care Research (NIHR) Maudsley Biomedical Research Centre (BRC). MLL is supported by R21NS087472, R01NS095937, R01AR079110, R01DA053316, R01DA047088.

For the purpose of open access, this paper has been published under a creative common licence (CC-BY) to any accepted author manuscript version arising from this submission. This study was funded by Medical Research Council-UK (MC_U120097115; MR/W005557/1 and MR/V013734/1), UKRI (no. 10039412), EU (no. 101028661 and 101026235), Margaret Temple, King’s Challenge Fund, and Wellcome Trust (no. 094849/Z/10/Z; 227867/Z/23/Z) grants to Dr Howes and the National Institute for Health and Care Research (NIHR) Biomedical Research Centre at South London and Maudsley NHS Foundation Trust and King’s College London. The views expressed are those of the author(s) and not necessarily those of the NIHR or the Department of Health.

Acknowledgments

We would like to thank all the participants who took part in these imaging studies and all the scientists who, in the name of collaborative science, provided us access to their data. We want also to thank all the radio-pharmacy and nuclear medicine technologists.

Availability of data and materials

The data that support the findings of this study were obtained under license. Therefore, restrictions apply to their public availability, and the datasets are not publicly accessible. Data may be made available from the corresponding authors upon reasonable request and with permission from the data provider.

References

- Albrecht, D. S., Forsberg, A., Sandström, A., Bergan, C., Kadetoff, D., Protsenko, E., Lampa, J., Lee, Y. C., Höglund, C. O., Catana, C., Cervenka, S., Akeju, O., Lekander, M., Cohen, G., Halldin, C., Taylor, N., Kim, M., Hooker, J. M., Edwards, R. R., ... Loggia, M. L. (2019). Brain glial activation in fibromyalgia – A multi-site positron emission tomography investigation. *Brain, Behavior, and Immunity*, *75*, 72–83. <https://doi.org/10.1016/j.bbi.2018.09.018>
- Albrecht, D. S., Granziera, C., Hooker, J. M., & Loggia, M. L. (2016). In Vivo Imaging of Human Neuroinflammation. *ACS Chemical Neuroscience*, *7*(4), 470–483. <https://doi.org/10.1021/acschemneuro.6b00056>
- Albrecht, D. S., Kim, • M, Akeju, • O, Torrado-Carvajal, • A, Edwards, • R R, Zhang, • Y, Bergan, • C, Protsenko, • E, Kucyi, • A, Wasan, • A D, Hooker, • J M, Napadow, • V, & Loggia, • M L. (2021). The neuroinflammatory component of negative affect in patients with chronic pain. *Molecular Psychiatry*, *26*, 864–874. <https://doi.org/10.1038/s41380-019-0433-1>
- Alshelh, Z., Albrecht, D. S., Bergan, C., Akeju, O., Clauw, D. J., Conboy, L., Edwards, R. R., Kim, M., Lee, Y. C., Protsenko, E., Napadow, V., Sullivan, K., & Loggia, M. L. (2020). In-vivo imaging of neuroinflammation in veterans with Gulf War illness. *Brain, Behavior, and Immunity*, *87*, 498–507. <https://doi.org/10.1016/j.bbi.2020.01.020>
- Aricioglu, F., Ozkartal, C. S., Unal, G., Dursun, S., Cetin, M., & Müller, N. (2016). Neuroinflammation in schizophrenia: A critical review and the future. In *Klinik Psikofarmakoloji Bulteni* (Vol. 26, Number 4). <https://doi.org/10.5455/bcp.20161123044657>
- Azevedo, C. J., Cen, S. Y., Khadka, S., Liu, S., Kornak, J., Shi, Y., Zheng, L., Hauser, S. L., & Pelletier, D. (2018). Thalamic atrophy in multiple sclerosis: A magnetic resonance imaging marker of

neurodegeneration throughout disease. *Annals of Neurology*, 83(2), 223–234.
<https://doi.org/10.1002/ana.25150>

Baliki, M. N., Mansour, A. R., Baria, A. T., & Apkarian, A. V. (2014). Functional Reorganization of the Default Mode Network across Chronic Pain Conditions. *PLoS ONE*, 9(9), e106133.
<https://doi.org/10.1371/journal.pone.0106133>

Barzon, L., Maccioni, L., Moretto, M., Giacomel, A., Schubert, J. J., Cousins, O., Rosenzweig, I., Mizuno, Y., Marques, T. R., Harrison, N. A., Fryer, T., Bullmore, E. T., Mondelli, V., Pariante, C., Howes, O., Turkheimer, F. E., & Veronese, M. (2025). *Peripheral inflammation is associated with reduced influx of TSPO PET tracers into the brain: insights from a non-invasive mapping methodology*. <https://doi.org/10.21203/rs.3.rs-6648321/v2>

Bloomfield, P. S., Selvaraj, S., Veronese, M., Rizzo, G., Bertoldo, A., Owen, D. R., Bloomfield, M. A. P., Bonoldi, I., Kalk, N., Turkheimer, F., McGuire, P., de Paola, V., & Howes, O. D. (2016). Microglial Activity in People at Ultra High Risk of Psychosis and in Schizophrenia: An [¹¹C]PBR28 PET Brain Imaging Study. *American Journal of Psychiatry*, 173(1), 44–52.
<https://doi.org/10.1176/appi.ajp.2015.14101358>

Borlongan, C., Acosta, S., de la Pena, I., Tajiri, N., Kaneko, Y., Lozano, D., & Gonzales-Portillo, G. (2015). Neuroinflammatory responses to traumatic brain injury: etiology, clinical consequences, and therapeutic opportunities. *Neuropsychiatric Disease and Treatment*, 11, 97.
<https://doi.org/10.2147/NDT.S65815>

Brites, D., & Fernandes, A. (2015). Neuroinflammation and depression: Microglia activation, extracellular microvesicles and microRNA dysregulation. In *Frontiers in Cellular Neuroscience* (Vol. 9, Number DEC). <https://doi.org/10.3389/fncel.2015.00476>

Burgos, N., Cardoso, M. J., Thielemans, K., Modat, M., Pedemonte, S., Dickson, J., Barnes, A., Ahmed, R., Mahoney, C. J., Schott, J. M., Duncan, J. S., Atkinson, D., Arridge, S. R., Hutton, B. F., & Ourselin, S. (2014). Attenuation Correction Synthesis for Hybrid PET-MR Scanners: Application to Brain Studies. *IEEE Transactions on Medical Imaging*, 33(12), 2332–2341.
<https://doi.org/10.1109/TMI.2014.2340135>

- Cai, M., Ma, J., Wang, Z., Zhao, Y., Zhang, Yijing, Wang, H., Xue, H., Chen, Y., Zhang, Yujie, Wang, C., Zhao, Q., Xue, K., Liu, F., & Feng Liu, C. (2023). Individual-level brain morphological similarity networks: Current methodologies and applications. *CNS Neurosci Ther*, *29*, 3713–3724. <https://doi.org/10.1111/cns.14384>
- Chang, P. C., Pollema-Mays, S. L., Centeno, M. V., Procissi, D., Contini, M., Baria, A. T., Martina, M., & Apkarian, A. V. (2014). Role of nucleus accumbens in neuropathic pain: Linked multi-scale evidence in the rat transitioning to neuropathic pain. *Pain*, *155*(6). <https://doi.org/10.1016/j.pain.2014.02.019>
- Chard, D. T., Jackson, J. S., Miller, D. H., & Wheeler-Kingshott, C. A. M. (2010). Reducing the Impact of White Matter Lesions on Automated Measures of Brain Gray and White Matter Volumes. *J. Magn. Reson. Imaging*, *32*, 223–228. <https://doi.org/10.1002/jmri.22214>
- Cheng, J.-C. K., Bevington, C. W. J., & Sossi, V. (2022). HYPR4D kernel method on TOF PET data with validations including image-derived input function. *EJNMMI Physics*, *9*(1), 78. <https://doi.org/10.1186/s40658-022-00507-6>
- Clarke, M. A., Archer, D., Yoon, K., Oguz, I., Smith, S. A., Xu, J., Cutter, G., & Bagnato, F. (2022). White matter tracts that overlap with the thalamus and the putamen are protected against multiple sclerosis pathology. *Multiple Sclerosis and Related Disorders*, *57*, 103430. <https://doi.org/10.1016/j.msard.2021.103430>
- Dahoun, T., Calcia, M. A., Veronese, M., Bloomfield, P., Reis Marques, T., Turkheimer, F., & Howes, O. D. (2019). The association of psychosocial risk factors for mental health with a brain marker altered by inflammation: A translocator protein (TSPO) PET imaging study. *Brain, Behavior, and Immunity*, *80*. <https://doi.org/10.1016/j.bbi.2019.05.023>
- De Picker, L. J., & Haarman, B. C. M. (2021). Applicability, potential and limitations of TSPO PET imaging as a clinical immunopsychiatry biomarker. In *European Journal of Nuclear Medicine and Molecular Imaging* (Vol. 49, Number 1). <https://doi.org/10.1007/s00259-021-05308-0>

- DeLisi, L. E., Szulc, K. U., Bertisch, H. C., Majcher, M., & Brown, K. (2006). Understanding structural brain changes in schizophrenia. *Dialogues in Clinical Neuroscience*, 8(1). <https://doi.org/10.31887/dcons.2006.8.1/ldelisi>
- DiSabato, D. J., Quan, N., & Godbout, J. P. (2016). Neuroinflammation: the devil is in the details. *Journal of Neurochemistry*, 139(S2), 136–153. <https://doi.org/10.1111/jnc.13607>
- Doorduyn, J., De Vries, E. F. J., Willemsen, A. T. M., De Groot, J. C., Dierckx, R. A., & Klein, H. C. (2009). Neuroinflammation in schizophrenia-related psychosis: A PET study. *Journal of Nuclear Medicine*, 50(11). <https://doi.org/10.2967/jnumed.109.066647>
- Farras-Permanyer, L., Mancho-Fora, N., Montalà-Flaquer, M., Bartrés-Faz, D., Vaqué-Alcázar, L., Peró-Cebollero, M., & Guàrdia-Olmos, J. (2019). Age-related changes in resting-state functional connectivity in older adults. *Neural Regeneration Research*, 14(9). <https://doi.org/10.4103/1673-5374.255976>
- Fjell, A. M., Sneve, M. H., Grydeland, H., Storsve, A. B., & Walhovd, K. B. (2017). The disconnected brain and executive function decline in aging. *Cerebral Cortex*, 27(3). <https://doi.org/10.1093/cercor/bhw082>
- Gerhard, A., Neumaier, B., Flitok, E., Glatting, G., Ries, V., Tomczak, R., Ludolph, A. C., & Reske, S. N. (2000). In vivo imaging of activated microglia using [11 C]PK11195 and positron emission tomography in patients after ischemic stroke. *NeuroReport*, 11(13), 2957–2960. <https://doi.org/10.1097/00001756-200009110-00025>
- Gerhard, A., Pavese, N., Hotton, G., Turkheimer, F., Es, M., Hammers, A., Eggert, K., Oertel, W., Banati, R. B., & Brooks, D. J. (2006). In vivo imaging of microglial activation with [11C](R)-PK11195 PET in idiopathic Parkinson's disease. *Neurobiology of Disease*, 21(2), 404–412. <https://doi.org/10.1016/j.nbd.2005.08.002>
- Goldin, P. R., McRae, K., Ramel, W., & Gross, J. J. (2008). The Neural Bases of Emotion Regulation: Reappraisal and Suppression of Negative Emotion. *Biological Psychiatry*, 63(6). <https://doi.org/10.1016/j.biopsych.2007.05.031>

- Gunn, R. N., Coello, C., & Searle, G. E. (2016). Molecular imaging and kinetic analysis toolbox (MIAKAT) - a quantitative software package for the analysis of PET neuroimaging data. *Journal of Nuclear Medicine*, 57(supplement 2).
- Harris, H., & Peng, Y. (2020). Evidence and explanation for the involvement of the nucleus accumbens in pain processing. *Neural Regeneration Research*, 15(4), 597. <https://doi.org/10.4103/1673-5374.266909>
- Heneka, M. T., Carson, M. J., Khoury, J. El, Landreth, G. E., Brosseron, F., Feinstein, D. L., Jacobs, A. H., Wyss-Coray, T., Vitorica, J., Ransohoff, R. M., Herrup, K., Frautschy, S. A., Finsen, B., Brown, G. C., Verkhratsky, A., Yamanaka, K., Koistinaho, J., Latz, E., Halle, A., ... Kummer, M. P. (2015). Neuroinflammation in Alzheimer's disease. *The Lancet Neurology*, 14(4), 388–405. [https://doi.org/10.1016/S1474-4422\(15\)70016-5](https://doi.org/10.1016/S1474-4422(15)70016-5)
- Holmes, S. E., Hinz, R., Conen, S., Gregory, C. J., Matthews, J. C., Anton-Rodriguez, J. M., Gerhard, A., & Talbot, P. S. (2018). Elevated Translocator Protein in Anterior Cingulate in Major Depression and a Role for Inflammation in Suicidal Thinking: A Positron Emission Tomography Study. *Biological Psychiatry*, 83(1), 61–69. <https://doi.org/10.1016/j.biopsych.2017.08.005>
- Howes, O. D., Bukala, B. R., & Beck, K. (2024). Schizophrenia: from neurochemistry to circuits, symptoms and treatments. *Nature Reviews Neurology*, 20(1), 22–35. <https://doi.org/10.1038/s41582-023-00904-0>
- Howes, O. D., & Onwordi, E. C. (2023). The synaptic hypothesis of schizophrenia version III: a master mechanism. *Molecular Psychiatry*, 28(5), 1843–1856. <https://doi.org/10.1038/s41380-023-02043-w>
- Howes, O., McCutcheon, R., & Stone, J. (2015). Glutamate and dopamine in schizophrenia: An update for the 21st century. In *Journal of Psychopharmacology* (Vol. 29, Number 2). <https://doi.org/10.1177/0269881114563634>
- Jain, P., Chaney, A. M., Carlson, M. L., Jackson, I. M., Rao, A., & James, M. L. (2020). Neuroinflammation PET Imaging: Current Opinion and Future Directions. *Journal of Nuclear Medicine*, 61(8), 1107–1112. <https://doi.org/10.2967/jnumed.119.229443>

- Kim, E. J., & Yu, S. W. (2015). Translocator protein 18 kDa (TSPO): Old dogma, new mice, new structure, and new questions for neuroprotection. *Neural Regeneration Research*, *10*(6). <https://doi.org/10.4103/1673-5374.158338>
- Krämer, J., Meuth, S., Tenberge, J.-G., Schiffler, P., Wiendl, H., & Deppe, M. (2015). Early and Degressive Putamen Atrophy in Multiple Sclerosis. *International Journal of Molecular Sciences*, *16*(10), 23195–23209. <https://doi.org/10.3390/ijms161023195>
- Kreutzberg, G. W. (1996). Microglia: A sensor for pathological events in the CNS. In *Trends in Neurosciences* (Vol. 19, Number 8). [https://doi.org/10.1016/0166-2236\(96\)10049-7](https://doi.org/10.1016/0166-2236(96)10049-7)
- Laaksonen, S., Saraste, M., Nylund, M., Hinz, R., Snellman, A., Rinne, J., Matilainen, M., & Airas, L. (2024). Sex-driven variability in TSPO-expressing microglia in MS patients and healthy individuals. *Frontiers in Neurology*, *15*. <https://doi.org/10.3389/fneur.2024.1352116>
- Laaksonen, S., Saraste, M., Sucksdorff, M., Nylund, M., Vuorimaa, A., Matilainen, M., Heikkinen, J., & Airas, L. (2023). Early prognosticators of later TSPO-PET-measurable microglial activation in multiple sclerosis. *Multiple Sclerosis and Related Disorders*, *75*, 104755. <https://doi.org/10.1016/j.msard.2023.104755>
- Lammertsma, A. A., & Hume, S. P. (1996). Simplified Reference Tissue Model for PET Receptor Studies. *NeuroImage*, *4*(3), 153–158. <https://doi.org/10.1006/NIMG.1996.0066>
- Leung, K.-K., Lee, T. M. C., Wong, M. M. C., Li, L. S. W., Yip, P. S. F., & Khong, P.-L. (2009). Neural correlates of attention biases of people with major depressive disorder: a voxel-based morphometric study. *Psychological Medicine*, *39*(7), 1097–1106. <https://doi.org/10.1017/S0033291708004546>
- Liu, J., Liao, X., Xia, M., & He, Y. (2018). Chronnectome fingerprinting: Identifying individuals and predicting higher cognitive functions using dynamic brain connectivity patterns. *Human Brain Mapping*, *39*(2), 902–915. <https://doi.org/10.1002/hbm.23890>

- Liu, X., Wang, Y., Ji, H., Aihara, K., & Chen, L. (2016). Personalized characterization of diseases using sample-specific networks. *Nucleic Acids Research*, *44*(22), e164–e164. <https://doi.org/10.1093/nar/gkw772>
- Liu, Y., Liang, P., Duan, Y., Huang, J., Ren, Z., Jia, X., Dong, H., Ye, J., Shi, F.-D., Butzkueven, H., & Li, K. (2015). Altered thalamic functional connectivity in multiple sclerosis. *European Journal of Radiology*, *84*(4), 703–708. <https://doi.org/10.1016/j.ejrad.2015.01.001>
- Loggia, M. L. (2024). “Neuroinflammation”: does it have a role in chronic pain? Evidence from human imaging. *Pain*, *165*(11S), S58–S67. <https://doi.org/10.1097/j.pain.0000000000003342>
- Loggia, M. L., Chonde, D. B., Akeju, O., Arabasz, G., Catana, C., Edwards, R. R., Hill, E., Hsu, S., Izquierdo-Garcia, D., Ji, R.-R., Riley, M., Wasan, A. D., Zürcher, N. R., Albrecht, D. S., Vangel, M. G., Rosen, B. R., Napadow, V., & Hooker, J. M. (2015). Evidence for brain glial activation in chronic pain patients. *Brain*, *138*(3), 604–615. <https://doi.org/10.1093/brain/awu377>
- Loggia, M. L., Kim, J., Gollub, R. L., Vangel, M. G., Kirsch, I., Kong, J., Wasan, A. D., & Napadow, V. (2013). Default mode network connectivity encodes clinical pain: An arterial spin labeling study. *Pain*, *154*(1), 24–33. <https://doi.org/10.1016/j.pain.2012.07.029>
- Lu, W., Song, T., Li, J., Zhang, Y., & Lu, J. (2024). Individual-specific metabolic network based on 18F-FDG PET revealing multi-level aberrant metabolisms in Parkinson’s disease. *Human Brain Mapping*, *45*(14), e70026. <https://doi.org/10.1002/hbm.70026>
- Maccioni, L., Brusaferrri, L., Barzon, L., Schubert, J. J., Netti, M. A., Cousins, O., Rosenzweig, I., Mizuno, Y., Vicente-Rodríguez, M., Singh, N., Marques, T. R., Harrison, N. A., Fryer, T., Bullmore, E. T., Cash, D., Mondelli, V., Pariante, C., Howes, O., Turkheimer, F. E., ... Veronese, M. (2025). A novel blood-free analytical framework for the quantification of neuroinflammatory load from TSPO PET imaging. *Journal of Cerebral Blood Flow & Metabolism*. <https://doi.org/10.1177/0271678X251361261>
- Maccioni, L., Michelle, C. M., Brusaferrri, L., Silvestri, E., Bertoldo, A., Schubert, J. J., Netti, M. A., Mondelli, V., Howes, O., Turkheimer, F. E., Bottlaender, M., Bodini, B., Stankoff, B., Loggia, M. L., & Veronese, M. (2024). A blood-free modeling approach for the quantification of the

blood-to-brain tracer exchange in TSPO PET imaging. *Frontiers in Neuroscience*, 18, 1395769. <https://doi.org/10.3389/fnins.2024.1395769>

Makary, M. M., Polosecki, P., Cecchi, G. A., DeAraujo, I. E., Barron, D. S., Constable, T. R., Whang, P. G., Thomas, D. A., Mowafi, H., Small, D. M., & Geha, P. (2020). Loss of nucleus accumbens low-frequency fluctuations is a signature of chronic pain. *Proceedings of the National Academy of Sciences*, 117(18), 10015–10023. <https://doi.org/10.1073/pnas.1918682117>

Malloy, P., & Aloia, M. (1998). Frontal Lobe Dysfunction in Traumatic Brain Injury. *Seminars in Clinical Neuropsychiatry*, 3(3), 186–194. <http://www.ncbi.nlm.nih.gov/pubmed/10085206>

Malpetti, M., Franzmeier, N., & Brendel, M. (2024). *PET Imaging to Measure Neuroinflammation In Vivo* (pp. 177–193). https://doi.org/10.1007/978-1-0716-3774-6_12

Marques, T. R., Ashok, A. H., Pillinger, T., Veronese, M., Turkheimer, F. E., Dazzan, P., Sommer, I. E. C., & Howes, O. D. (2019). Neuroinflammation in schizophrenia: meta-analysis of in vivo microglial imaging studies. *Psychological Medicine*, 49(13), 2186–2196. <https://doi.org/10.1017/S0033291718003057>

Marques, T. R., Veronese, M., Owen, D. R., Rabiner, E. A., Searle, G. E., & Howes, O. D. (2021). Specific and non-specific binding of a tracer for the translocator-specific protein in schizophrenia: an [11C]-PBR28 blocking study. *European Journal of Nuclear Medicine and Molecular Imaging*, 48(11), 3530–3539. <https://doi.org/10.1007/s00259-021-05327-x>

McAllister, T. W. (2011). Neurobiological consequences of traumatic brain injury. *Dialogues in Clinical Neuroscience*, 13(3), 287–300. <https://doi.org/10.31887/DCNS.2011.13.2/tmcallister>

McCutcheon, R. A., Abi-Dargham, A., & Howes, O. D. (2019). Schizophrenia, Dopamine and the Striatum: From Biology to Symptoms. *Trends in Neurosciences*, 42(3), 205–220. <https://doi.org/10.1016/j.tins.2018.12.004>

McCutcheon, R. A., Krystal, J. H., & Howes, O. D. (2020). Dopamine and glutamate in schizophrenia: biology, symptoms and treatment. *World Psychiatry*, 19(1), 15–33. <https://doi.org/10.1002/wps.20693>

- McInnes, L., Healy, J., Saul, N., & Großberger, L. (2018). UMAP: Uniform Manifold Approximation and Projection. *Journal of Open Source Software*, 3(29). <https://doi.org/10.21105/joss.00861>
- Morrissey, E. J., Alshelh, Z., Knight, P. C., Saha, A., Kim, M., Torrado-Carvajal, A., Zhang, Y., Edwards, R. R., Pike, C., Locascio, J. J., Napadow, V., & Loggia, M. L. (2023). Assessing the potential anti-neuroinflammatory effect of minocycline in chronic low back pain: Protocol for a randomized, double-blind, placebo-controlled trial. *Contemporary Clinical Trials*, 126, 107087. <https://doi.org/10.1016/j.cct.2023.107087>
- Mubarik, A., & Tohid, H. (2016). Frontal lobe alterations in schizophrenia: a review. *Trends in Psychiatry and Psychotherapy*, 38(4), 198–206. <https://doi.org/10.1590/2237-6089-2015-0088>
- Müller, N. (2018). Inflammation in Schizophrenia: Pathogenetic Aspects and Therapeutic Considerations. *Schizophrenia Bulletin*, 44(5), 973–982. <https://doi.org/10.1093/schbul/sby024>
- Nair, A., Veronese, M., Xu, X., Curtis, C., Turkheimer, F., Howard, R., & Reeves, S. (2016). Test-retest analysis of a non-invasive method of quantifying [11C]-PBR28 binding in Alzheimer's disease. *EJNMMI Research*, 6(1), 72. <https://doi.org/10.1186/s13550-016-0226-3>
- Nutma, E., Ceyzériat, K., Amor, S., Tsartsalis, S., Millet, P., Owen, D. R., Papadopoulos, V., & Tournier, B. B. (2021). Cellular sources of TSPO expression in healthy and diseased brain. *European Journal of Nuclear Medicine and Molecular Imaging*, 49(1), 146–163. <https://doi.org/10.1007/s00259-020-05166-2>
- Nutma, E., Fancy, N., Weinert, M., Tsartsalis, S., Marzin, M. C., Muirhead, R. C. J., Falk, I., Breur, M., de Bruin, J., Hollaus, D., Pieterman, R., Anink, J., Story, D., Chandran, S., Tang, J., Trolese, M. C., Saito, T., Saido, T. C., Wiltshire, K. H., ... Owen, D. R. (2023). Translocator protein is a marker of activated microglia in rodent models but not human neurodegenerative diseases. *Nature Communications*, 14(1). <https://doi.org/10.1038/s41467-023-40937-z>
- Owen, D. R., Yeo, A. J., Gunn, R. N., Song, K., Wadsworth, G., Lewis, A., Rhodes, C., Pulford, D. J., Bennacef, I., Parker, C. A., StJean, P. L., Cardon, L. R., Mooser, V. E., Matthews, P. M., Rabiner, E. A., & Rubio, J. P. (2012). An 18-kDa Translocator Protein (TSPO) Polymorphism Explains

Differences in Binding Affinity of the PET Radioligand PBR28. *Journal of Cerebral Blood Flow & Metabolism*, 32(1), 1–5. <https://doi.org/10.1038/jcbfm.2011.147>

Pedregosa, F., Varoquaux, G., Gramfort, A., Michel, V., Thirion, B., Grisel, O., Blondel, M., Prettenhofer, P., Weiss, R., Dubourg, V., Vanderplas, J., Passos, A., Cournapeau, D., Brucher, M., Perrot, M., & Duchesnay, É. (2011). Scikit-learn: Machine learning in Python. *Journal of Machine Learning Research*, 12.

Protas, H., Ghisays, V., Goradia, D. D., Bauer, R., Devadas, V., Chen, K., Reiman, E. M., & Su, Y. (2023). Individualized network analysis: A novel approach to investigate tau PET using graph theory in the Alzheimer's disease continuum. *Frontiers in Neuroscience*, 17, 1089134. <https://doi.org/10.3389/fnins.2023.1089134>

Radlinska, B. A., Ghinani, S. A., Lyon, P., Jolly, D., Soucy, J.-P., Minuk, J., Schirmacher, R., & Thiel, A. (2009). Multimodal Microglia Imaging of Fiber Tracts in Acute Subcortical Stroke. *Ann Neurol*, 66, 825–832. <https://doi.org/10.1002/ana.21796>

Rauchmann, B., Brendel, M., Franzmeier, N., Trappmann, L., Zaganjori, M., Ersoezlue, E., Morenas-Rodriguez, E., Guersel, S., Burow, L., Kurz, C., Haeckert, J., Tatò, M., Utecht, J., Papazov, B., Pogarell, O., Janowitz, D., Buerger, K., Ewers, M., Palleis, C., ... Perneczky, R. (2022). Microglial Activation and Connectivity in Alzheimer Disease and Aging. *Annals of Neurology*, 92(5), 768–781. <https://doi.org/10.1002/ana.26465>

Richards, E. M., Zanotti-Fregonara, P., Fujita, M., Newman, L., Farmer, C., Ballard, E. D., Machado-Vieira, R., Yuan, P., Niciu, M. J., Lyoo, C. H., Henter, I. D., Salvatore, G., Drevets, W. C., Kolb, H., Innis, R. B., & Zarate, C. A. (2018). PET radioligand binding to translocator protein (TSPO) is increased in unmedicated depressed subjects. *EJNMMI Research*, 8. <https://doi.org/10.1186/s13550-018-0401-9>

Rizzo, G., Veronese, M., Tonietto, M., Bodini, B., Stankoff, B., Wimberley, C., Lavisse, S., Bottlaender, M., Bloomfield, P. S., Howes, O., Zanotti-Fregonara, P., Turkheimer, F. E., & Bertoldo, A. (2019). Generalization of endothelial modelling of TSPO PET imaging:

Considerations on tracer affinities. *Journal of Cerebral Blood Flow and Metabolism*, 39(5).
<https://doi.org/10.1177/0271678X17742004>

Rodriguez-Mogeda, C., Koubiyr, I., Prouskas, S. E., Georgallidou, M., van der Pol, S. M. A., Fernandez, R. F., de Graaf, Y. G., van der Werf, Y. D., Jonkman, L. E., Schenk, G. J., Barkhof, F., Hulst, H. E., Witte, M. E., Schoonheim, M. M., & de Vries, H. E. (2025). Thalamic atrophy in multiple sclerosis is associated with tract disconnection and altered microglia. *Acta Neuropathologica*, 149(1), 52. <https://doi.org/10.1007/s00401-025-02893-4>

Sala, A., Lizarraga, A., Caminiti, S. P., Calhoun, V. D., Eickhoff, S. B., Habeck, C., Jamadar, S. D., Perani, D., Pereira, J. B., Veronese, M., & Yakushev, I. (2023). Brain connectomics: time for a molecular imaging perspective? *Trends in Cognitive Sciences*, 27(4), 353–366. <https://doi.org/10.1016/j.tics.2022.11.015>

Schmaal, L., Hibar, D. P., Sämann, P. G., Hall, G. B., Baune, B. T., Jahanshad, N., Cheung, J. W., van Erp, T. G. M., Bos, D., Ikram, M. A., Vernooij, M. W., Niessen, W. J., Tiemeier, H., Hofman, A., Wittfeld, K., Grabe, H. J., Janowitz, D., Bülow, R., Selonke, M., ... Veltman, D. J. (2017). Cortical abnormalities in adults and adolescents with major depression based on brain scans from 20 cohorts worldwide in the ENIGMA Major Depressive Disorder Working Group. *Molecular Psychiatry*, 22(6), 900–909. <https://doi.org/10.1038/mp.2016.60>

Schoonheim, M. M., Pinter, D., Prouskas, S. E., Broeders, T. A., Pirpamer, L., Khalil, M., Ropele, S., Uitdehaag, B. M., Barkhof, F., Enzinger, C., & Geurts, J. J. (2022). Disability in multiple sclerosis is related to thalamic connectivity and cortical network atrophy. *Multiple Sclerosis Journal*, 28(1), 61–70. <https://doi.org/10.1177/13524585211008743>

Schubert, J. J., Veronese, M., Fryer, T. D., Manavaki, R., Kitzbichler, M. G., Nettis, M. A., Mondelli, V., Pariante, C. M., Bullmore, E. T., Turkheimer, F. E., Wlazly, D., Dickinson, A., Foster, A., Knight, C., Leckey, C., Morgan, P., Morgan, A., O'Hagan, C., Touchard, S., ... Mount, H. (2021). A Modest Increase in 11C-PK11195-Positron Emission Tomography TSPO Binding in Depression Is Not Associated With Serum C-Reactive Protein or Body Mass Index. *Biological Psychiatry: Cognitive Neuroscience and Neuroimaging*, 6(7), 716–724. <https://doi.org/10.1016/j.bpsc.2020.12.017>

- Schubert, J., Tonietto, M., Turkheimer, F., Zanotti-Fregonara, P., & Veronese, M. (2021). Supervised clustering for TSPO PET imaging. In *European Journal of Nuclear Medicine and Molecular Imaging* (Vol. 49, Number 1). <https://doi.org/10.1007/s00259-021-05309-z>
- Schuitmaker, A., Kropholler, M. A., Boellaard, R., van der Flier, W. M., Kloet, R. W., van der Doef, T. F., Knol, D. L., Windhorst, A. D., Luurtsema, G., Barkhof, F., Jonker, C., Lammertsma, A. A., Scheltens, P., & van Berckel, B. N. M. (2013). Microglial activation in Alzheimer's disease: an (R)-[11C]PK11195 positron emission tomography study. *Neurobiology of Aging*, *34*(1), 128–136. <https://doi.org/10.1016/j.neurobiolaging.2012.04.021>
- Scott, G., Zetterberg, H., Jolly, A., Cole, J. H., De Simoni, S., Jenkins, P. O., Feeney, C., Owen, D. R., Lingford-Hughes, A., Howes, O., Patel, M. C., Goldstone, A. P., Gunn, R. N., Blennow, K., Matthews, P. M., & Sharp, D. J. (2018). Minocycline reduces chronic microglial activation after brain trauma but increases neurodegeneration. *Brain*, *141*(2), 459–471. <https://doi.org/10.1093/brain/awx339>
- Sebenius, I., Seidlitz, J., Warriar, V., Bethlehem, R. A. I., Alexander-Bloch, A., Mallard, T. T., Garcia, R. R., Bullmore, E. T., & Morgan, S. E. (2023). Robust estimation of cortical similarity networks from brain MRI. *Nature Neuroscience*, *26*(8), 1461–1471. <https://doi.org/10.1038/s41593-023-01376-7>
- Setiawan, E., Attwells, S., Wilson, A. A., Mizrahi, R., Rusjan, P. M., Miler, L., Xu, C., Sharma, S., Kish, S., Houle, S., & Meyer, J. H. (2018). Association of translocator protein total distribution volume with duration of untreated major depressive disorder: a cross-sectional study. *The Lancet Psychiatry*, *5*(4), 339–347. [https://doi.org/10.1016/S2215-0366\(18\)30048-8](https://doi.org/10.1016/S2215-0366(18)30048-8)
- Severino, M., Peretti, D. E., Bardiau, M., Cavaliere, C., Doyen, M., Gonzalez-Escamilla, G., Horowitz, T., Nørgaard, M., Perez, J. A. M., Perovnik, M., Rullmann, M., Steenken, D., Talmasov, D., Tang, C., Volpi, T., Xu, Z., Bertoldo, A., Calhoun, V. D., Caminiti, S. P., ... Veronese, M. (2025). Molecular connectivity studies in neurotransmission: a scoping review. *Imaging Neuroscience*, *3*. https://doi.org/10.1162/imag_a_00530

- Severino, M., Schubert, J. J., Nordio, G., Giacomel, A., Easmin, R., Lao-Kaim, N. P., Selvaggi, P., Xu, Z., Pereira, J. B., Jauhar, S., Piccini, P., Howes, O., Turkheimer, F., & Veronese, M. (2025). Single-Subject Network Analysis of FDOPA PET in Parkinson's Disease and Psychosis Spectrum. *Human Brain Mapping*, *46*(8), e70253. <https://doi.org/10.1002/hbm.70253>
- Sucksdorff, M., Matilainen, M., Tuisku, J., Polvinen, E., Vuorimaa, A., Rokka, J., Nylund, M., Rissanen, E., & Airas, L. (2020). Brain TSPO-PET predicts later disease progression independent of relapses in multiple sclerosis. *Brain*, *143*(11), 3318–3330. <https://doi.org/10.1093/brain/awaa275>
- Suh, J. S., Schneider, M. A., Minuzzi, L., MacQueen, G. M., Strother, S. C., Kennedy, S. H., & Frey, B. N. (2019). Cortical thickness in major depressive disorder: A systematic review and meta-analysis. *Progress in Neuro-Psychopharmacology and Biological Psychiatry*, *88*, 287–302. <https://doi.org/10.1016/j.pnpbp.2018.08.008>
- Talbot, P. S., & Cooper, S. J. (2006). Anterior cingulate and subgenual prefrontal blood flow changes following tryptophan depletion in healthy males. *Neuropsychopharmacology*, *31*(8). <https://doi.org/10.1038/sj.npp.1301022>
- Tonietto, M., Rizzo, G., Veronese, M., Fujita, M., Zoghbi, S. S., Zanotti-Fregonara, P., & Bertoldo, A. (2016). Plasma radiometabolite correction in dynamic PET studies: Insights on the available modeling approaches. In *Journal of Cerebral Blood Flow and Metabolism* (Vol. 36, Number 2). <https://doi.org/10.1177/0271678X15610585>
- Torrado-Carvajal, A., Toschi, N., Albrecht, D. S., Chang, K., Akeju, O., Kim, M., Edwards, R. R., Zhang, Y., Hooker, J. M., Duggento, A., Kalpathy-Cramer, J., Napadow, V., & Loggia, M. L. (2021). Thalamic neuroinflammation as a reproducible and discriminating signature for chronic low back pain. *Pain*, *162*(4), 1241–1249. <https://doi.org/10.1097/j.pain.0000000000002108>
- Tournier, B. B., Tsartsalis, S., Ceyzériat, K., Garibotto, V., & Millet, P. (2020). In Vivo TSPO Signal and Neuroinflammation in Alzheimer's Disease. *Cells*, *9*(9), 1941. <https://doi.org/10.3390/cells9091941>

- Troubat, R., Barone, P., Leman, S., Desmidt, T., Cressant, A., Atanasova, B., Brizard, B., El Hage, W., Surget, A., Belzung, C., & Camus, V. (2021). Neuroinflammation and depression: A review. *European Journal of Neuroscience*, *53*(1), 151–171. <https://doi.org/10.1111/ejn.14720>
- Tuisku, J., Plavén-Sigraý, P., Gaiser, E. C., Airas, L., Al-Abdulrasul, H., Brück, A., Carson, R. E., Chen, M.-K., Cosgrove, K. P., Ekblad, L., Esterlis, I., Farde, L., Forsberg, A., Halldin, C., Helin, S., Kosek, E., Lekander, M., Lindgren, N., Marjamäki, P., ... Cervenka, S. (2019). Effects of age, BMI and sex on the glial cell marker TSPO — a multicentre [11C]PBR28 HRRT PET study. *European Journal of Nuclear Medicine and Molecular Imaging*, *46*(11), 2329–2338. <https://doi.org/10.1007/s00259-019-04403-7>
- Turkheimer, F. E., Althubaity, N., Schubert, J., Nettis, M. A., Cousins, O., Dima, D., Mondelli, V., Bullmore, E. T., Pariante, C., & Veronese, M. (2021). Increased serum peripheral C-reactive protein is associated with reduced brain barriers permeability of TSPO radioligands in healthy volunteers and depressed patients: implications for inflammation and depression. *Brain, Behavior, and Immunity*, *91*, 487–497. <https://doi.org/10.1016/j.bbi.2020.10.025>
- Turkheimer, F. E., Rizzo, G., Bloomfield, P. S., Howes, O., Zanotti-Fregonara, P., Bertoldo, A., & Veronese, M. (2015). The methodology of TSPO imaging with positron emission tomography. *Biochemical Society Transactions*, *43*(4), 586–592. <https://doi.org/10.1042/BST20150058>
- Veronese, M., Moro, L., Arcolin, M., Dipasquale, O., Rizzo, G., Expert, P., Khan, W., Fisher, P. M., Svarer, C., Bertoldo, A., Howes, O., & Turkheimer, F. E. (2019). Covariance statistics and network analysis of brain PET imaging studies. *Scientific Reports*, *9*(1), 2496. <https://doi.org/10.1038/s41598-019-39005-8>
- Veronese, M., Reis Marques, T., Bloomfield, P. S., Rizzo, G., Singh, N., Jones, D., Agushi, E., Mosses, D., Bertoldo, A., Howes, O., Roncaroli, F., & Turkheimer, F. E. (2018). Kinetic modelling of [11C]PBR28 for 18 kDa translocator protein PET data: A validation study of vascular modelling in the brain using XBD173 and tissue analysis. *Journal of Cerebral Blood Flow & Metabolism*, *38*(7), 1227–1242. <https://doi.org/10.1177/0271678X17712388>

- Vicente-Rodríguez, M., Singh, N., Turkheimer, F., Peris-Yague, A., Randall, K., Veronese, M., Simmons, C., Karim Haji-Dheere, A., Bordoloi, J., Sander, K., Awais, R. O., Årstad, E., NIMA Consortium, Cash, D., & Parker, C. A. (2021). Resolving the cellular specificity of TSPO imaging in a rat model of peripherally-induced neuroinflammation. *Brain, Behavior, and Immunity*, 96. <https://doi.org/10.1016/j.bbi.2021.05.025>
- Volpi, T., Maccioni, L., Colpo, M., Debiassi, G., Capotosti, A., Ciceri, T., Carson, R. E., DeLorenzo, C., Hahn, A., Knudsen, G. M., Lammertsma, A. A., Price, J. C., Sossi, V., Wang, G., Zanotti-Fregonara, P., Bertoldo, A., & Veronese, M. (2023). An update on the use of image-derived input functions for human PET studies: new hopes or old illusions? *EJNMMI Research*, 13(1), 97. <https://doi.org/10.1186/s13550-023-01050-w>
- Volpi, T., Vallini, G., Silvestri, E., Francisci, M. De, Durbin, T., Corbetta, M., Lee, J. J., Vlassenko, A. G., Goyal, M. S., & Bertoldo, A. (2023). A new framework for metabolic connectivity mapping using bolus [18F]FDG PET and kinetic modeling. *Journal of Cerebral Blood Flow and Metabolism: Official Journal of the International Society of Cerebral Blood Flow and Metabolism*, 43(11), 1905–1918. <https://doi.org/10.1177/0271678X231184365>
- Wang, H., Jin, X., Zhang, Y., & Wang, J. (2016). Single-subject morphological brain networks: connectivity mapping, topological characterization and test–retest reliability. *Brain and Behavior*, 6(4), e00448. <https://doi.org/10.1002/brb3.448>
- Wang, M., Jiang, J., Yan, Z., Alberts, I., Ge, J., Zhang, H., Zuo, C., Yu, J., Rominger, A., & Shi, K. (2020). Individual brain metabolic connectome indicator based on Kullback-Leibler Divergence Similarity Estimation predicts progression from mild cognitive impairment to Alzheimer’s dementia. *European Journal of Nuclear Medicine and Molecular Imaging*, 47(12), 2753–2764. <https://doi.org/10.1007/s00259-020-04814-x>
- Werry, E. L., Bright, F. M., Piguet, O., Ittner, L. M., Halliday, G. M., Hodges, J. R., Kiernan, M. C., Loy, C. T., Kril, J. J., & Kassiou, M. (2019). Recent Developments in TSPO PET Imaging as A Biomarker of Neuroinflammation in Neurodegenerative Disorders. *International Journal of Molecular Sciences*, 20(13), 3161. <https://doi.org/10.3390/ijms20133161>

- Wijesinghe, S. S., Rowe, J. B., Mason, H. D., Allinson, K. S. J., Thomas, R., Vontobel, D. S., Fryer, T. D., Hong, Y. T., Bacioglu, M., Spillantini, M. G., van den Ameele, J., O'Brien, J. T., Kaalund, S., Malpetti, M., & Quaegebeur, A. (2025). Post-mortem validation of *in vivo* TSPO PET as a microglial biomarker. *Brain*. <https://doi.org/10.1093/brain/awaf078>
- Yang, S., & Chang, M. C. (2019). Chronic Pain: Structural and Functional Changes in Brain Structures and Associated Negative Affective States. *International Journal of Molecular Sciences*, *20*(13), 3130. <https://doi.org/10.3390/ijms20133130>
- Yong, V. W. (2022). Microglia in multiple sclerosis: Protectors turn destroyers. *Neuron*, *110*(21), 3534–3548. <https://doi.org/10.1016/j.neuron.2022.06.023>
- Yu, K., Wang, X., Li, Q., Zhang, X., Li, X., & Li, S. (2018). Individual Morphological Brain Network Construction Based on Multivariate Euclidean Distances Between Brain Regions. *Frontiers in Human Neuroscience*, *12*, 204. <https://doi.org/10.3389/fnhum.2018.00204>
- Zhang, F. F., Peng, W., Sweeney, J. A., Jia, Z. Y., & Gong, Q. Y. (2018). Brain structure alterations in depression: Psychoradiological evidence. In *CNS Neuroscience and Therapeutics* (Vol. 24, Number 11). <https://doi.org/10.1111/cns.12835>
- Zhu, Z., Zhang, Z., Gao, X., Feng, L., Chen, D., Yang, Z., & Hu, S. (2022). Individual Brain Metabolic Connectome Indicator Based on Jensen-Shannon Divergence Similarity Estimation Predicts Seizure Outcomes of Temporal Lobe Epilepsy. *Frontiers in Cell and Developmental Biology*, *9*, 803800. <https://doi.org/10.3389/fcell.2021.803800>